The chemistry and structure of calcium (alumina) silicate hydrate: A study by XANES, ptychographic imaging, and wide- and small-angle scattering

The Chemistry and Structure of Calcium (Alumino) Silicate Hydrate: A Study by XANES, Ptychographic Imaging, and Wide- and Small- Angle Scattering

Jiaqi Li[a,*], Guoqing Geng[a,b,*] , Rupert Myers[a,c], Young-Sang Yu[d], David Shapiro[d], Carlo Carraro[e], Roya Maboudian[e], and Paulo J.M. Monteiro[a,f]

[a] Department of Civil and Environmental Engineering, University of California, Berkeley, California, United States

[b] Paul Scherrer Institute, Villigen, Switzerland

[c] School of Engineering, University of Edinburgh, Edinburgh, United Kingdom

[d] Advanced Light Source, Lawrence Berkeley National Laboratory, Berkeley, California, United States

[e] Department of Chemical and Biomolecular Engineering, University of California, Berkeley, California, United States

[f] Material Science Division, Lawrence Berkeley National Laboratory, Berkeley, California, United States

Abstract

Calcium (alumino)silicate hydrate (C-(A-)S-H) is the main binding phase in blended cement concrete. Understanding the chemistry and structure of C-(A-)S-H is essential to optimizing concrete properties such as compressive strength and durability; yet questions remain around the coordination environments of Ca and Al in its structure with various chemical compositions and equilibration temperatures. C-(A-)S-H with Ca/Si = 0.6-1.6, Al/Si = 0-0.1, and equilibrated at 7-80°C are studied by nanoscale soft X-ray spectroscopy at the Ca $L_{2,3}$- and Si *K*-edges. Highly distorted CaO_7 complexes occur in

* Corresponding authors
E-mail address: Jiaqi.li@berkeley.edu (J. Li) guoqing_geng@berkeley.edu (G. Geng)
Postal address: 115 Davis Hall, University of California at Berkeley, Berkeley, California, USA, 94720

the intralayer of C-(A-)S-H irrespective of Ca/Si, Al/Si, and temperature. Zeolitic Ca in the interlayer of C-(A-)S-H are highly distorted from an ideal octahedral coordination. Third aluminate hydrate is either not Ca-bearing or its Ca is structurally similar to C-(A-)S-H and does not resemble the Ca in AFm-phases. Increasing aluminosilicate chain polymerization in C-(A-)S-H shifts the Si *K*-edge to higher energies, implying Al uptake in the bridging and/or cross-linked sites, as well as a contraction of Si-O bond lengths. C-(A-)S-H exhibits a foil-like morphology, with individual foils comprised of nano-sized platelets with comparable thickness regardless of Ca/Si or Al/Si at 7-50°C. Coarser C-(A-)S-H foils occur at 80°C and higher Al/Si ratios relative to lower temperatures and Al content.

Keywords

Temperature, calcium-silicate-hydrate, third aluminate hydrate, blended cement, C-A-S-H

1.Introduction

Calcium (alumino)silicate hydrate (C-(A-)S-H) [†] is the main binding phase in blended cement concrete[1]. The Ca/Si ratio in calcium silicate hydrate (C-S-H) in hydrated Portland cement (PC) is ~1.7 [2]. The addition of supplementary cementitious materials (SCMs), e.g., fly ash and blast furnace slag, leads to the uptake of Al and a decrease in Ca/(Si+Al) ratio in this phase [3, 4]. C-(A-)S-H equilibrated at room temperature is

[†] Cement chemistry shorthand notation is used throughout the text: A, Al_2O_3; C, CaO; H, H_2O; S, SiO_2; and $\overline{S}$, SO_3.

58 structurally analogous to defective tobermorite, which contains calcium oxide polyhedra
59 sheets flanked with “dreierketten” – tetrahedral (alumino)silicate chains – on one side and
60 counter-ions (e.g., Ca and alkalis) and water in an interlayer on the other [5-9]. At
61 Ca/Si<0.6-0.8, long silicate tetrahedral chains occur, which predominantly consist of
62 repeating units of one bridging site (Q^2_B) ‡ connected to two paired silicate tetrahedral
63 sites (Q^2_P) on either side. At higher Ca/Si ratios >~1.0 these chains are significantly
64 shorter albeit structurally similar, and have varying degrees of vacant tetrahedra in
65 bridging sites [10].

66

67 Aluminum incorporated into these chains occur in tetrahedral AlO_4 sites. Five-fold
68 coordinated aluminum (Al^V) and six-fold coordinated Al (Al^{VI-a}) have also been
69 identified to occur in C-(A-)S-H [11-13]. Increased availability of Al favors the
70 precipitation of katoite (C_3AH_6) and strätlingite (C_2ASH_8) as secondary products, which
71 become increasingly stable relative to Al uptake in C-(A-)S-H at higher Al concentrations.
72 These conditions also promote the precipitation of octahedral Al (Al^{VI-b}) in a (calcium)
73 aluminate hydrate phase (also termed as the third aluminum hydrate, TAH) [14-16]. The
74 nature and location of this phase remain unclear. Substitution of Si for Al in C-A-S-H
75 occurs preferably in bridging sites. Si for Al substitution also occurs in cross-linked
76 bridging sites (Q^3) at 80 °C, and in alkali-activated fly ash and slag at room temperature
77 [12, 17-19]. Note that, the solubility and coordination of Al are pH dependent; the pH of
78 pore solution of hardened concrete typically is 13-14 [20].

‡ Here, $Q^n(m\text{Al})$ designates a SiO_4 tetrahedron that is connected to m AlO_4 tetrahedra and n aluminosilicate tetrahedra.

One major continuing debate in existing C-S-H models [21-25] is the coordination of Ca in C-S-H. An extended X-ray absorption fine structure (EXAFS) study showed that Ca is octahedrally coordinated in C-S-H at Ca/Si ratios of 0.7-1.4, and in 11 Å and 14 Å tobermorite [26], the results do not agree with XRD data of tobermorite [27]. XRD results from Merlino and Bonacorrsi [5-9, 27-30] clearly showed that the coordination number of Ca of 11Å- and 14Å- tobermorite is seven and/or six. Kirkpatrick et al. [31] reported distinct values for the average coordination numbers of Ca: 5.5-6.2 for C-S-H(I), 6.1 for 11 Å tobermorite, and 6.9 for 14 Å tobermorite. A pair distribution function (PDF) study showed that the average coordination number of Ca in synthetic C-S-H systematically decreases from 7.1 to 6.0 as Ca/Si ratio increases [32]. ^{43}Ca nuclear magnetic resonance (NMR) analysis showed that Ca environments in C-S-H are similar to 11 Å tobermorite at Ca/Si $\leq$ 1.5 [33]. A C-S-H model with octahedral Ca-O sheet for accommodating Al was proposed [22]. Coordination numbers of Ca in thirty five crystalline C-S-H and related minerals were mainly found to be six or seven, with a small number of eight-fold Ca atoms [34]. There is consensus that the coordination number of Ca in C-S-H is between 6 and 7 although it remains unclear how the coordination symmetry of CaO_x complexes varies with Al incorporation and equilibration temperature.

Transmission electron microscopy (TEM) studies have shown that 'outer product' C-S-H is fibrillar in hydrated PC pastes and foil like in hydrated PC-slag blends [2, 23, 35-38]. The morphology of C-S-H with various Ca/Si and equilibration conditions varies from

101 foil to fiber-like [39]. However, the effects of chemical compositions and equilibration
102 temperatures on the morphology of synthetic C-A-S-H have not been extensively studied.
103 The sample preparation and high accelerating voltage of TEM can damage C-(A-)S-H
104 samples [40], limiting its use in characterizing these materials. Ptychographic imaging
105 using synchrotron-based X-ray radiation has only relatively recently been applied to
106 characterize the morphology of cement-based materials [41, 42]. It yields image
107 resolutions of 10 nm or better while, for many materials, results in less damage compared
108 to TEM. Coupled with scanning transmission X-ray microscopy (STXM), it enables
109 comprehensive nanometer-resolved spectroscopic investigation of cementitious materials.
110 Preliminary STXM studies have shown a strong correlation between the degree of
111 polymerization of silicate chains and features in X-ray Absorption Near Edge Structure
112 (XANES) spectra at the Si *K*-edge [43-45]. However, more experimental work is needed
113 to obtain Si *K*-edge XANES spectra of C-(A-)S-H covering the full range of
114 compositions and temperatures applicable to hydrated PC/SCM blends.

115

116 This paper aims to use STXM, coupled with ptychographic imaging, to provide new
117 insights into the effects of bulk Ca/Si molar ratios (0.6-1.6), bulk Al/Si molar ratios (0-
118 0.1), and equilibration temperatures at 7, 20, 50, and 80 °C on the atomic environment of
119 Ca, Si, and Al in C-(A-)S-H. The experimental setup here provides state-of-the-art
120 spatially resolved (~10 nm) chemical information of C-(A-)S-H and intermixed
121 secondary phases. Results are used to unveil the chemistry and nano-morphology of these
122 phases, and also correlate the degree of polymerization of its (alumino)silicate chains
123 with features in Ca $L_{2,3}$- and Si *K*-edges XANES spectra.

2. Materials and methods

2.1. Materials

C-(A-)S-H samples were synthesized at initial bulk Ca/Si molar ratios (Ca/Si*) of 0.6, 0.8, 1.0, 1.2, 1.4 and 1.6, bulk Al/Si molar ratios (Al/Si*) of 0 and 0.05, and cured at 20 °C for 182 days by mixing stoichiometric amounts of SiO_2 (Aerosil 200, Evonik), CaO (prepared by calcining $CaCO_3$ (Merck Millipore) at 1000 °C for 12 h) and $CaO{\cdot}Al_2O_3$ at a water/solid ratio of 45 in a N_2-filled glove box. Additional samples with Ca/Si* = 1 and Al/Si* of 0, 0.05 and 0.1 were water bathed at 7 °C for one year, and at 50 and 80°C for 56 days. The solid C-(A-)S-H samples were vacuum filtered by using 0.45 μm nylon filter papers, freeze-dried for 7 days, and then stored in N_2-filled desiccators in the presence of saturated $CaCl_2$ solutions and NaOH pellets. Full details of these procedures are provided in [46].

2.2. Methods

2.2.1. XANES/STXM

XANES spectra of the C-(A-)S-H samples were obtained using STXM at bending magnet beamlines 5.3.2.1 and 5.3.2.2 at the Advanced Light Source (ALS) of the Lawrence Berkeley National Laboratory (LBNL) [47]. The STXM beamlines use synchrotron X-ray radiation as the incident beam. The monochromatic X-ray is focused using a zone plate onto the samples that are mounted on a multi-motor stage inside a vacuum chamber (base pressure of 200 mTorr). The downstream phosphor-photomultiplier tube (PMT) records the transmitted X-ray intensity as a function of the tuned beam energy.

147 Depending on the scanning mode, e.g., line-scan and area-scan, the absorption data of the
148 scanned locations can be generated and assessed using suitable software, e.g., A*xis2000*
149 [45]. In this study, XANES spectra at Si *K*-edge (1830-1880 eV) were measured in line
150 scan mode with an energy resolution of 0.3 eV and a dwell time of 50 ms; spectra at Ca
151 $L_{2,3}$-edge (345-356 eV) were obtained in line scan mode at an energy resolution of 0.1 eV
152 with a dwell time of 30 ms. A comprehensive description of the STXM beamlines is
153 given in [48].

154

155 **2.2.2. X-ray Ptychography**

156 X-ray ptychographic images were obtained at 800 eV at beamline 5.3.2.1 at ALS, using
157 the STXM setup described above except a fast CCD detector was used. Details of the
158 imaging method are reported in [39]. In brief, it uses scanning steps smaller than the
159 beam spot, i.e., the adjacent illuminated spots are greatly overlapped. The cluster-based
160 codes reconstruct both the real and imaginary parts of the transmitted X-ray beam in each
161 scanning step, which then yield high-resolution images using either magnitude or phase
162 information as the contrast. The pixel size in this study is 5 nm, although the actual
163 spatial resolution (smallest resolvable features as determined by the amount of scattering
164 from the sample) is estimated to be ~10 nm. To avoid X-ray beam absorption saturation,
165 the C-(A-)S-H samples were gently dispersed in polystyrene weigh boats (Fisherbrand)
166 using isopropanol (>99.5% purity, Fisher Chemical) with liquid-to-solid mass ratio of 10
167 and dropped in between two Si_3N_4 windows (100-nm-thick, Norcada). To quantify the
168 morphological information obtained using ptychography, we integrated small angle

scattering (SAS) by calculating small angle scattering patterns from the ptychographic magnitude images. A lamellar Guinier–Porod model was used to fit the patterns, which enable the sizes of the C-(A-)S-H particles to be estimated. More details are shown in Supplementary Information.

3. Results and discussion

3.1. Ca coordination

3.1.1. Ca/Si* = 0.6-1.6, Al/Si* = 0, and equilibrium at 20 °C

The Ca $L_{2,3}$-edge spectra of the C-(A-)S-H samples (Figures 1 and 2) resemble $L_{2,3}$-edge spectra of d^0 compounds, e.g., Ca^{2+} and K^+. They correspond to the excitation of Ca atoms from $2p^6 3d^0$ to $2p^5 3d^1$. Due to the loss of degeneracy of $2p$ orbitals by spin-orbit coupling, two major peaks are observed, L_3 ($2p_{3/2}$, a_2 peak) and L_2 ($2p_{1/2}$, b_2 peak) [49]. Minor peaks (a_1 and b_1) exist to the left of each major peak, which originate from crystal field splitting. These peaks are clearly observed when the coordination configuration is of a certain symmetry, e.g., octahedral or cubic. The energy separations (splitting energies, $\Delta L_3 = a_2 - a_1$ and $\Delta L_2 = b_2 - b_1$) in two doublets between the adjacent major and minor peaks relate to the strength of the crystal field effects, which depend on the ligand type and distortion of the symmetry [50]. A small leading peak a_0 originates from the mixing of states due to multipole interactions of core holes with valence electrons, combined with $3d$ spin-orbit splitting effects [51].

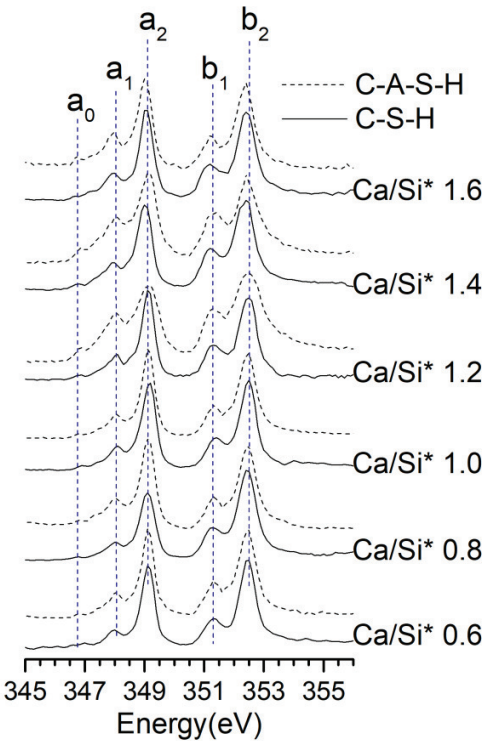

191

192

193 **Figure 1.** Ca $L_{2,3}$-edge XANES spectra of C-S-H (solid lines) and C-A-S-H with Al/Si* =

194 0.05 (dashed lines) after 182 days of hydration at 20 °C. Ca/Si* = bulk Ca/Si

195

196 The spectra indicate that Ca possesses an octahedral-like coordination symmetry in all

197 samples. However, this symmetry is clearly distorted since the a_1 and b_1 peaks are not as

198 sharp and intense as those in $Ca(OH)_2$ spectra, where Ca is in an ideal octahedral

199 symmetry. The pre-edge peak a_0 is less resolvable in C-S-H samples than in C-A-S-H

200 samples due to the poorer crystallinity of C-S-H. The Ca in the studied samples are not

201 cubic-coordinated, else an extra minor peak would be visible between a_1 and a_2 peaks

202 (katoite-like) [52].

For samples with Ca/Si* in the range of 0.6-1.4, the splitting energies of C-S-H are consistently near 1.1 eV (see **Error! Reference source not found.**), suggesting that most Ca in C-S-H are in similar coordination environments. The low peak intensity ratios between minor and major peaks suggest that there is no tendency to form a well-crystallized phase as Ca/Si increases [43, 49, 53, 54]. In addition, a strong splitting is not observed in C-S-H with Ca/Si* = 1.6 when the scanned step is refined to ~20 nm. The absence of strong splitting suggests that the small amount of portlandite in bulk X-ray diffraction (XRD) results [46] forms distinct (micro)crystallites, and does not regularly intermix with C-(A-)S-H at the length scale of 20 nm. This interpretation is consistent with the previous assignment of a Ca/Si ratio of 1.38 to this C-S-H phase in this sample, with the remaining Ca in this sample assigned to a distinct portlandite phase (Ca/Si* = 1.6) [55]. Our results are also consistent with the interpretation that the Ca/Si* = 1.6 sample is not fully equilibrated [56], because at this composition and at equilibrium phase pure C-S-H is stable [57]. Therefore, the Ca $L_{2,3}$-edge spectra are fully explained by a defective tobermorite based model [58], i.e., the low splitting energy at Ca $L_{2,3}$-edge originates mainly from the seven-fold coordinated Ca-O sheet in the intralayer of C-S-H, and has minor contribution from the octahedral coordinated zeolitic Ca that is charge-balanced in the interlayer. As Ca/Si increases, there is no increasing trend of the peak intensity ratios between minor and major peaks, indicating that the increasing amount of the interlayer Ca is six-fold coordinated in a highly distorted octahedral symmetry, which is consistent with our interpretation. The interlayer $[Ca(H_2O)_6]^{2+}$ at Ca/Si $\leq$ 1.5 and $[Ca(OH)(H_2O)_5]^{+}$ at Ca/Si* = 1.6 suggested by Gartner et al. [59] are both with highly

226 distorted octahedral symmetry, which is consistent with our interpretation. Furthermore,
227 the PDF work reported that the interlayer Ca in C-S-H with high Ca/Si ratios (>1.2) is
228 more likely octahedrally coordinated [32].
229
230 The major peak positions (a_2 and b_2) in the spectra for C-S-H with Ca/Si* = 0.6-1.2 are
231 generally equivalent, suggesting a comparable oxidation degree of Ca and a similar
232 average coordination number of Ca-O in C-S-H at low Ca/Si*. For Ca/Si* of 1.4 and 1.6,
233 the major peak positions are 0.05-0.1 eV lower than those at Ca/Si* ≤ 1.2, suggesting that
234 more six-fold coordinated zeolitic Ca species are charge-balanced in the interlayer or on
235 the surface of C-S-H in this higher Ca/Si* range. The occurrence of seven- and/or six-
236 fold Ca sites in C-S-H(I) is in good agreement with 11Å- and 14Å-tobermorite, the Ca-O
237 coordination numbers of which are mostly six or seven [5, 27, 34]. The reported X-ray
238 photoelectron spectroscopy experiments exhibit similar results, namely, a Ca $2p_{3/2}$
239 binding energy of C-S-H [60] that is independent of the Ca/Si ratio.
240
241 **3.1.2. Ca/Si* = 0.6-1.6, Al/Si* = 0.05, and equilibrium at 20 °C**
242 Comparable peak positions are identified in the Ca $L_{2,3}$-edge spectra for the C-A-S-H and
243 C-S-H samples equilibrated at 20 °C, indicating that minor Al uptake (Al/Si* = 0.05)
244 does not greatly alter the coordination of Ca-O complexes in their structures, regardless
245 of Ca/Si ratio. At Ca/Si* = 1.4 and 1.6, the major peaks in the C-A-S-H spectra are
246 positioned at slightly higher energies than in the C-S-H spectra. We assign this effect to
247 the higher ordering of CaO_7 due to Al incorporation by elongating silicate chains and
248 CaO_7 sheets. Compared to the peak intensity ratios (a_1/a_2 and b_1/b_2) of C-S-H, the C-A-S-

H spectra exhibit marginally higher values, which suggests an increase in the long-range order of CaO_7 sheet due to Al incorporation. However, Al incorporation does not increase the coordination symmetry of Ca-O complexes in C-(A-)S-H structure since its splitting energies are still comparable to C-S-H.

Figure 2 shows the Ca $L_{2,3}$-edge XANES spectra of Ca-O complexes in C-(A-)S-H and in other cement-related phases [41]. Katoite was reported to form in the C-A-S-H samples that were analyzed here by L'Hôpital et al. using bulk XRD, thermogravimetric analysis, and ^{27}Al NMR measurements [56]. Yet the absence of the additional peak (a_{1o}) in this C-A-S-H phase on the sub-20 nm scale suggests that katoite does not intermix with C-A-S-H on this length scale. The major peak positions (a_2 and b_2) on C-A-S-H samples are identical to C_2AH_8 and monosulfate ($C_4A\overline{S}H_{12}$), which both have Ca coordination numbers of seven, and the major peak positions are ~0.2 eV lower than CAH_{10} and ettringite ($C_6A\overline{S}_3H_{32}$), which have Ca coordination numbers of eight. Therefore, we assign the coordination number of Ca in the CaO_x sheet of C-A-S-H to seven – the average coordination number of Ca in C-A-S-H is thus slightly smaller than seven due to the existence of minor quantities of octahedral Ca in the interlayer.

The absence of the leading a_{1o} and b_{1o} peaks in the Ca $L_{2,3}$-edge spectra, which are the characteristic peaks of AFm phases, AFm-like phases do not exist in C-A-S-H products. Furthermore, the Ca-O(H) complexes in C-A-S-H interlayer or on its surface are in octahedral-like coordination, although highly distorted. Renaudin et al. [61] proposed that calcium hydroxide, aluminum hydroxide, and an AFm-type calcium aluminate hydrate

main layer may form in the interlayer of C-A-S-H. Andersen et al. [62] proposed that phases with octahedral Al may precipitate on C-A-S-H surfaces or as separate phases. The type of Ca found in AFm-type calcium aluminate hydrates is not identified in our Ca $L_{2,3}$-edge spectra on the sub-20nm scale, indicating that TAH is not Ca-bearing or its Ca coordination environment is structurally analogous to Ca in C-(A-)S-H.

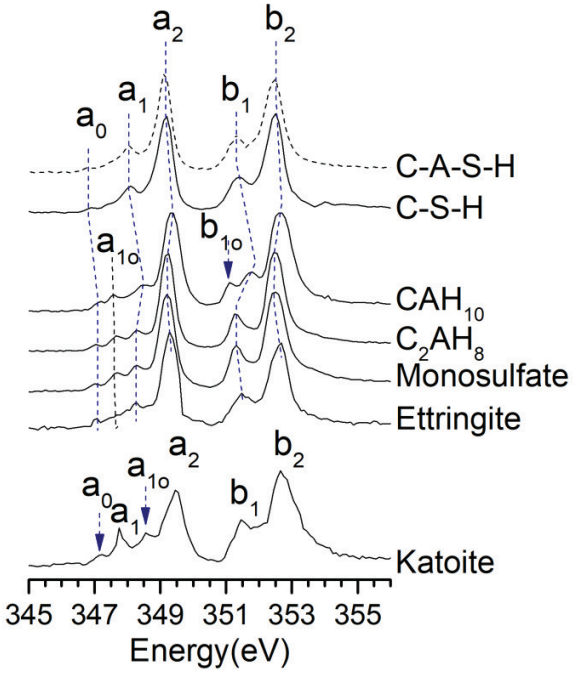

Figure 2. Ca $L_{2,3}$-edge XANES spectra of C-S-H (solid lines) and C-A-S-H (dashed lines, Al/Si* = 0.05) after 182 days of hydration at 20°C. Spectra of CAH_{10}, C_2AH_8, monosulfoaluminate (monosulfate, $C_4A\bar{S}H_{12}$), ettringite ($C_6A\bar{S}_3H_{32}$) and katoite (C_3AH_6) are taken from [41]. Ca/Si* = bulk Ca/Si.

3.1.3. Ca/Si* = 1, Al/Si* = 0-0.1, and equilibrium at 7-80 °C

The peak positions in the Ca $L_{2,3}$-edge spectra for the C-(A-)S-H samples equilibrated at temperature ranging from 7 to 80 °C are found to be similar (Figure 3 and Table 1). Therefore, the coordination numbers of Ca-O complexes in these samples are independent of equilibration temperature in this range. The coordination symmetry of

288 Ca^{2+} in the interlayer of C-(A-)S-H is also clearly distorted regardless of the equilibration
289 temperature. The slight increase in the relative intensity of minor to major peaks (a_1/a_2
290 and b_1/b_2) with increasing equilibration temperature is observed in this temperature
291 ranges and is attributed to increased long-range order of CaO_7 sheets in the C-(A-)S-H
292 structure; the increment is more pronounced at 80°C, indicating increased structural
293 ordering in this sample. This result is consistent with [46], where the degree of stacking
294 in the *c*-direction of C-(A-)S-H at 80°C was observed to significantly increase. At each
295 equilibration temperature, the relative intensity ratio of minor to major peaks slightly
296 increases as Al incorporation increases, which suggests that CaO_7 sheets in C-A-S-H are
297 more long range ordered than those in C-S-H. We attribute this effect to the more
298 polymerized aluminosilicate chains in the C-A-S-H samples.
299
300 **Table 1.** Features in the Ca $L_{2,3}$-edge XANES spectra of C-(A-)S-H samples. The
301 estimated absolute errors are ± 0.01 eV in energy positions and ± 0.0002 units in intensity
302 ratios.

Al/Si*	Ca/Si*	Energy (eV)								
		a_0	a_1	a_2	a_1/a_2	ΔL_3	b_1	b_2	b_1/b_2	ΔL_2
Equilibrium at 20°C										
0	0.6	347	348.0	349.1	0.0648	1.1	351.4	352.5	0.0944	1.1
	0.8	346.8	348.0	349.1	0.0618	1.1	351.35	352.45	0.0647	1.1
	1.0	348.8	348.0	349.1	0.0495	1.1	351.4	352.5	0.0756	1.1
	1.2	346.8	348.05	349.1	0.089	1.05	351.4	352.5	0.089	1.1
	1.4	346.8	347.95	349.0	0.0695	1.05	351.3	352.4	0.0935	1.1
	1.6	346.8	347.95	349.05	0.0842	1.1	351.25	352.4	0.1015	1.15
0.05	0.6	346.7	348.0	349.1	0.0992	1.1	351.4	352.5	0.1278	1.1
	0.8	346.8	348.0	349.1	0.0794	1.1	351.4	352.5	0.1382	1.1
	1.0	346.8	348.05	349.1	0.0798	1.05	351.45	352.5	0.1334	1.05
	1.2	346.8	348.0	349.1	0.144	1.1	351.4	352.5	0.1159	1.1
	1.4	346.8	348.0	349.1	0.0902	1.1	351.35	352.45	0.1501	1.1
	1.6	346.8	348.05	349.1	0.155	1.05	351.35	352.45	0.1482	1.1
Equilibrium at 7°C										
0	1.0	347*	348.0*	349.1	-	1.1	351.4	352.5	0.017	1.1

0.05	1.0	347*	348.0*	349.1	0.0134	1.1	351.4	352.5	0.053	1.1
0.1	1.0	346.8*	348.0*	349.1	0.0433	1.1	351.4	352.5	0.0856	1.1
Equilibrium at 50°C										
0	1.0	346.8	348.0	349.1	0.0814	1.1	351.35	352.5	0.0931	1.15
0.05	1.0	346.8	348.0	349.1	0.1188	1.1	351.4	352.5	0.1581	1.1
0.1	1.0	346.8	348.0	349.1	0.1303	1.1	351.4	352.5	0.171	1.1
Equilibrium at 80°C										
0	1.0	346.8	348.0	349.1	0.0861	1.1	351.4	352.5	0.1688	1.1
0.05	1.0	346.8	348.0	349.1	0.1458	1.1	351.4	352.5	0.2241	1.1
0.1	1.0	346.8	348.0	349.1	0.1718	1.1	351.4	352.5	0.2557	1.1

*weak peak, peak position is not clearly identified.

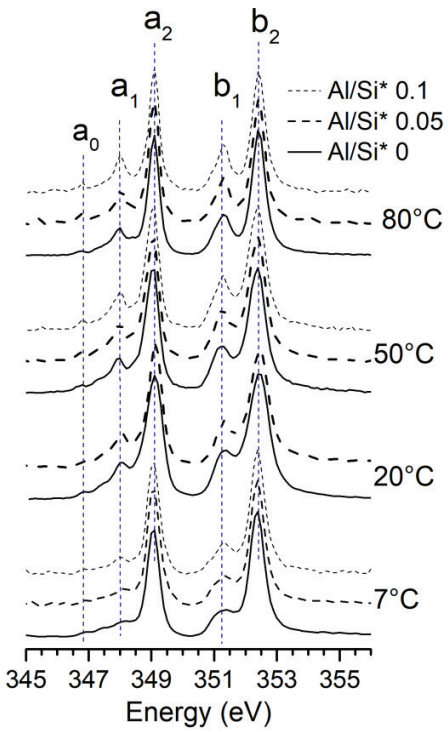

Figure 3. Ca $L_{2,3}$-edge XANES spectra of C-S-H (solid lines, Al/Si* = 0, Ca/Si* = 1.0), C-A-S-H (long-dashed lines, Al/Si* = 0.05, Ca/Si* = 1.0), and C-A-S-H (short-dashed lines, Al/Si* = 0.1, Ca/Si* = 1.0) at different equilibration temperatures. Ca/Si* = bulk Ca/Si. Al/Si* = bulk Al/Si.

313

314 **3.2. Chemical environment of Si**

315 **3.2.1. Ca/Si* = 0.6-1.6, Al/Si* = 0, and equilibrium at 20 °C**

316 Figure 4 shows the Si *K*-edge XANES spectra of C-(A-)S-H equilibrated at 20°C. The
317 major peak a_1 (Si *K*-edge peak) at 1848.7 – 1849.7 eV is assigned to the electronic
318 transition from 1*s* to antibonding 3*p*-like state (t_2) in tetrahedrally symmetric Si (dipole
319 allowed) [63]. The minor peaks a_2 (at ~1860-1867 eV) and a_3 (1853 eV) are attributable
320 to multi-scattering effect from more distant atom shells through photo-electron
321 interaction, particularly the second coordination shell, and its energy is governed by the
322 interatomic distance [64]. The peak positions and energy separation between a_1 and a_2
323 peaks are listed in Table 2. A pre-edge peak presenting the transition of Si 1*s* electrons to
324 the antibonding 3*s* orbital (dipole-forbidden) is only observed in the Ca/Si* = 1.6 C-S-H
325 sample, suggesting the distortion of tetrahedral sites in the silicate chains.

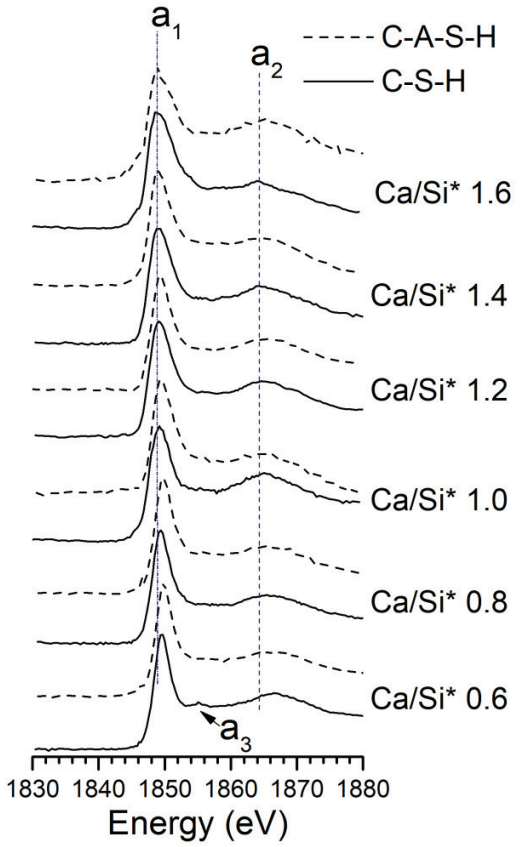

Figure 4. Si *K*-edge XANES spectra of C-S-H (solid lines) and C-A-S-H with Al/Si* = 0.05 (dashed lines) after 182 days of equilibration at 20 °C. Ca/Si* = bulk Ca/Si. Al/Si* = bulk Al/Si.

As the Ca/Si ratio increases, the Si *K*-edges gradually shift to lower energy by 1 eV (Figure 5). This effect is caused by the progressive increase in the electron shielding from more Ca and a reduction in the effective Si-O bond strength. The positive correlation between the location of the Si *K*-edge and the degree of silicate polymerization (i.e., mean chain length of silicate chains, MCL) in the C-S-H samples is consistent with previous work on silicate minerals [63, 65].

338 The major and minor peak positions (a_1 and a_2) of C-S-H increase as the Ca/Si ratio
339 decreases, suggesting a contraction of average Si-O bond lengths [66-69]. This trend is
340 consistent with PDF analysis which showed slightly decreased average Si-O bond lengths
341 as Ca/Si* decreases [32]. The inverse correlation between Si-O bond length and degree of
342 silicate polymerization in the C-S-H samples with varying Ca/Si ratio is consistent with
343 previous findings in many silicate minerals [69]. In general, the Si-O-Si bond angle is
344 inversely correlated to Si-O bond length [70] (and thus directly related to the degree of
345 silicate polymerization in C-S-H). Therefore, the shifted position of the Si *K*-edge to
346 higher energies here implies that Si-O-Si bond angles in C-S-H increases as Ca/Si
347 decreases. The Si *K*-edge peak a_1 sharpens with a decreased Ca/Si ratio, suggesting an
348 increased long-range ordering of silicate tetrahedra [71]. This interpretation is consistent
349 with previous studies on C-S-H materials, namely, as Ca/Si ratio decreases, (1) the
350 ordering of Si-O-Si bond angles increases [72]; (2) the Si-O-Si bond angle broadens [73];
351 (3) the Si $2p_{3/2}$ and 2*s* binding energies increase [60, 74]; and (4) the MCL of silicate
352 chains in C-S-H increases [10]. Therefore, the energy difference between a_1 and a_2 peaks
353 (Δa_2-a_1) correlates to changing degrees of polymerization in these silicate chains (Figure
354 5).
355

356 **3.2.2. Ca/Si* = 0.6-1.6, Al/Si* = 0.05, and equilibrium at 20°C**

357 The energies of the Si *K*-edges in the spectra for the C-A-S-H samples increase by 0.1 to
358 0.3 eV with respect to C-S-H samples at each Ca/Si ratio increment (i.e., from Ca/Si* =
359 0.6 to 0.8, etc.) due to the increase in degree of polymerization of aluminosilicate chains
360 (Figures 4 and 5). The trend of increasing MCL with increasing Al in C-(A-)S-H is well

known [13, 56]. As the MCL in C-(A-)S-H increases, the electron shielding on Si from zeolitic Ca decreases, which corresponds to Si atoms effectively becoming more negatively charged. Increasing energies of the positions of Si *K*-edges in the spectra imply slight contractions of Si-O bonds in C-(A-)S-H. At Ca/Si* = 1.4 and 1.6, the increment of Si *K*-edge of C-A-S-H compared to C-S-H is 0.2 and 0.3 eV, respectively, which is slightly greater than that of C-A-S-H at lower Ca/Si ratio. This implies that aluminate tetrahedra link silicate dimers together and that Al prefers to occupy bridging sites, a significant proportion of which are vacant in C-S-H at Ca/Si ratios > 1.

Cross-linked Q^3 species are not clearly identified in C-A-S-H samples equilibrated at 20 °C, which is consistent with ^{29}Si NMR results of the same samples [56]. The Si *K*-edge peak, a_1, (1849 eV -1849.8 eV) of C-A-S-H is broadened compared to C-S-H and corresponds to Q^2(1Al) sites. As mentioned before, the energy of Si *K*-edge is dependent on the Si-O bong length and on the degree of silicate polymerization, while the position of a_2 peak is governed by the interatomic distance [63, 71, 75, 76]. Therefore, the energy difference between the a_1 and a_2 peaks, Δa_2-a_1, is related to the degree of polymerization (i.e., MCL) and to the Si-O bond length of C-(A-)S-H. The ascending trends of Δa_2-a_1 and Si *K*-edge of C-A-S-H as the Ca/Si ratio decreases follows the same correlation of C-S-H, suggesting that the MCL increases with decreasing Ca/Si ratio. The value of Δa_2-a_1 in C-A-S-H at each Ca/Si ratio is also slightly larger than the value of Δa_2-a_1 in C-S-H (**Error! Reference source not found.**), which implies the increase in MCL by Al incorporation.

Table 2. Peak positions and energy differences of Si *K*-edge XANES spectra of C-(A-)S-H equilibrated at 20 °C. The estimated absolute errors are ± 0.05 units in positions of peak a_1 and at Ca/Si = 0.6-1.2, ± 0.1 units in position of peak a_1 at Ca/Si = 1.4- 1.6, and ± 0.15 units in position of peak a_2 and energy differences between peaks a_1 and a_2.

Ca/Si*	Peak a_1 (eV)	Peak a_2 (eV)	Δa_2-a_1 (eV)
Al/Si*=0			
0.6	1849.7	1866.6	16.9
0.8	1849.4	1865.6	16.2
1.0	1849.2	1865.1	15.9
1.2	1849.1	1864.8	15.7
1.4	1848.8	1864.6	15.4
1.6	1848.7	1864.0	15.3
Al/Si*=0.05			
0.6	1849.8	1866.9	17.1
0.8	1849.5	1865.9	16.4
1.0	1849.3	1865.4	16.1
1.2	1849.2	1865.1	15.9
1.4	1849.0	1864.8	15.8
1.6	1849.0	1864.6	15.6

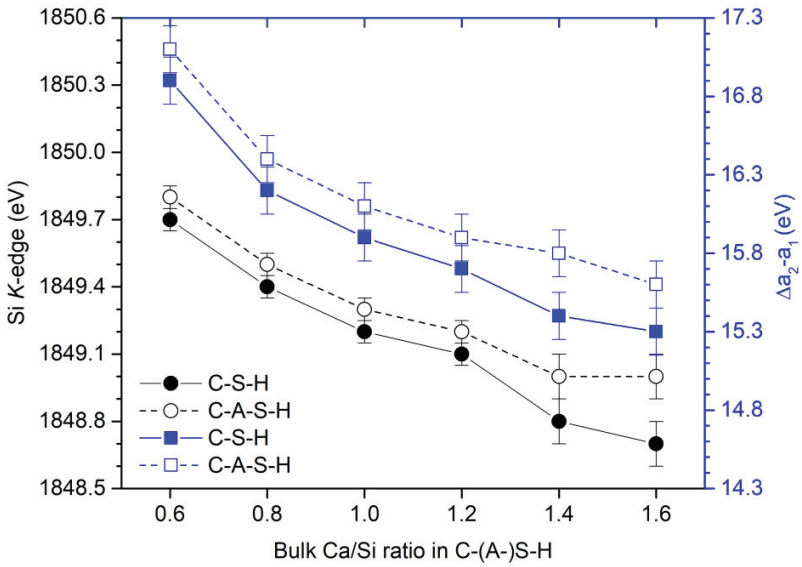

Figure 5. Si *K*-edge energy and energy separation between major and minor peak (Δa_2-a_1) as a function of Ca/Si* ratio of C-S-H (solid lines) and C-A-S-H with Al/Si* = 0.05 (dashed lines) after 182 days of equilibration at 20°C.

3.2.3 Ca/Si* = 1, Al/Si* = 0-0.1, and equilibrium at 7-80°C

394 At each equilibration temperature, in addition to the increase in energy difference, Δa_2-a_1,
395 the Si *K*-edge of C-(A-)S-H shifts to higher energy with increasing Al/Si* ratio (Figure 6
396 and Table 3). This suggests an elongation of aluminosilicates chains and marginal
397 shortening of Si-O bonds, both resulting from Al uptake. The shoulder at ~1853.8-1855.8
398 eV (peak a_4) suggests that Q^3 and/or Q^3(1Al) sites occur in the C-A-S-H sample
399 equilibrated at 80 °C [64]. The position of the Si *K*-edge of C-A-S-H is shifted to a
400 markedly higher energy at 80 °C due to the occurrence of these Q^3 and Q^3(1Al) sites. The
401 Si *K*-edge and Δa_2-a_1 do not systematically vary across the equilibration temperature
402 range of 7 to 80 °C, but do positively correlate with the MCL of C-(A-)S-H (Figure 7).
403 The trend is consistent with the relationship between the energies, Ca/Si ratio and MCL
404 of C-(A-)S-H at 20°C, i.e., the energies increase with increasing MCL and decreasing Si-
405 O bond length. Two distinct Si *K*-edge spectra are differentiated in C-S-H products
406 synthesized at 80 °C, which are assigned to tobermorite-like structures with average basal
407 spacing of 13.8 Å and 12.1 Å (See Table A1, Supplementary Information); the latter is
408 more abundant in the sample, which is consistent with [77]. The relatively higher Si *K*-
409 edge and Δa_2-a_1 of C-S-H with 13.8 Å average basal spacing suggests that it has a longer
410 MCL than the C-S-H phase with an average basal spacing of 12.1 Å.

411
412 **Table 3.** Features of Si *K*-edge XANES spectra for C-(A-)S-H samples (Ca/Si* = 1)
413 equilibrated at different temperatures. The estimated absolute errors are ± 0.05 units in
414 positions of peak a_1 for C-(A-)S-H equilibrated at 7 °C - 50 °C, ± 0.1 units in position of
415 peak a_1 at for C-(A-)S-H equilibrated at 80 °C, and ± 0.15 units in position of peak a_2 and
416 energy differences between peaks a_1 and a_2.

Al/Si*	Peak a_1 (eV)	Peak a_2 (eV)	Δa_2-a_1 (eV)
Equilibrium at 7°C			
0	1849.4	1865.3	15.9
0.05	1849.6	1865.6	16.0
0.1	1850.0	1866.2	16.2

Equilibrium at 20°C			
0	1849.2	1865.1	15.9
0.05	1849.3	1865.4	16.1
Equilibrium at 50°C			
0	1849.3	1865.1	15.8
0.05	1849.6	1865.7	16.1
0.1	1849.9	1866.1	16.2
Equilibrium at 80°C			
0 (12.1 Å)	1849.6	1865.6	16.0
0 (13.8 Å)	1849.7	1865.8	16.1
0.05	1850.2	1866.5	16.3
0.1	1850.4	1866.9	16.5

417 The basal spacing shown in parentheses was measured by wide-angle X-ray scattering
418 (WAXS, Appendix A in Supplementary Information). Al/Si* = bulk Al/Si.
419

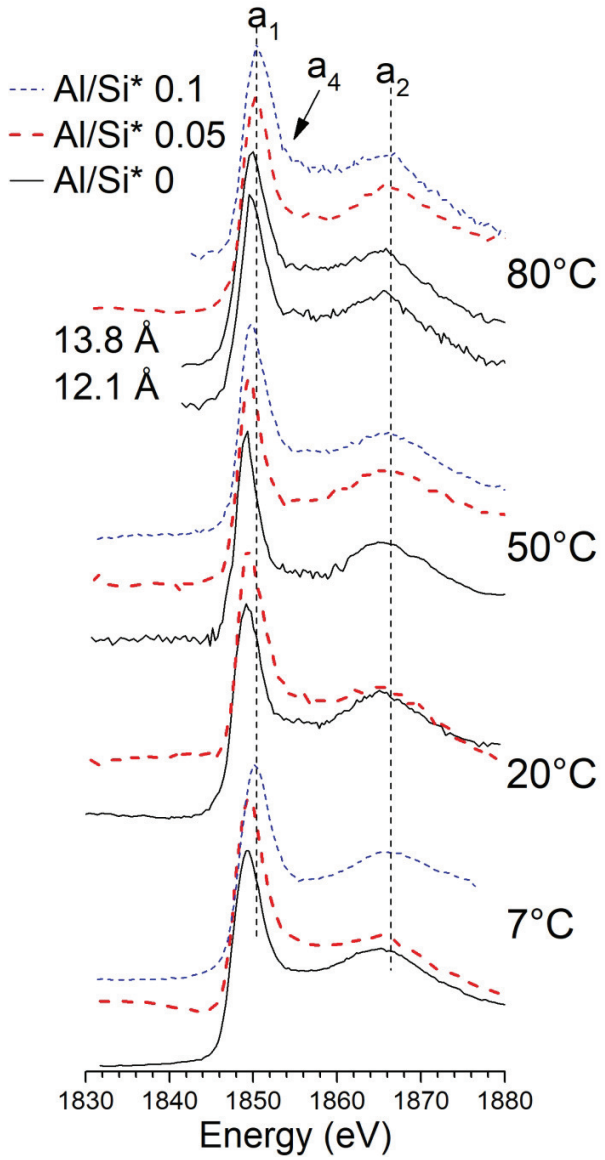

Figure 6. Si *K*-edge XANES spectra of C-S-H (solid lines, Ca/Si* = 1.0), C-A-S-H (red long-dashed lines, Al/Si* = 0.05, Ca/Si* = 1.0), and C-A-S-H (blue short-dashed lines, Al/Si* = 0.1, Ca/Si* = 1.0) at different equilibration temperatures. The two C-S-H phases exist in the 80 °C sample, which are labeled with their average basal spacings. Ca/Si* = bulk Ca/Si. Al/Si* = bulk Al/Si.

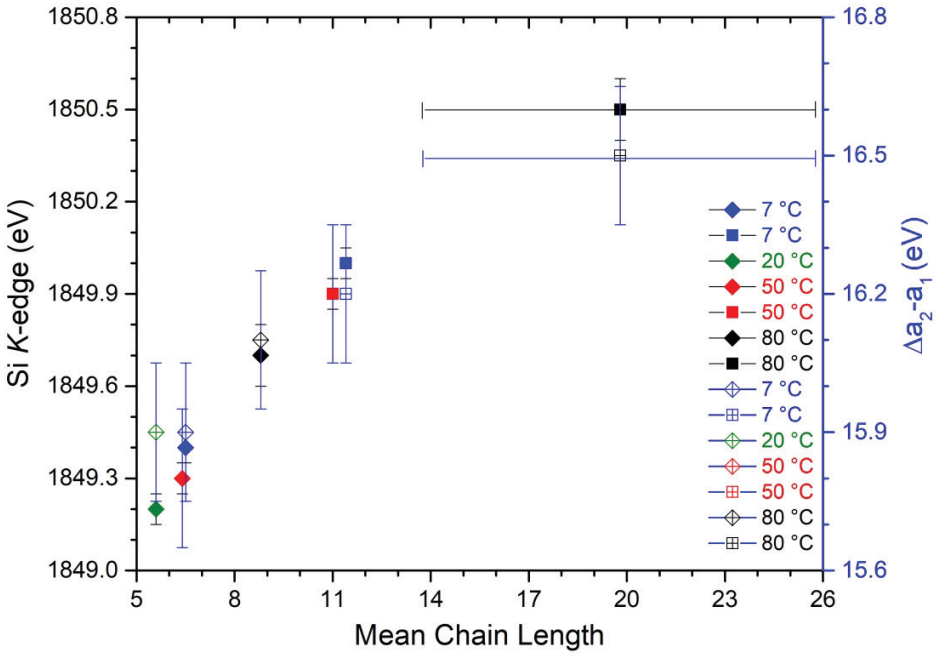

Figure 7. Si *K*-edge energy and energy separation between major and minor peak (Δa_2-a_1) as a function of the MCL of C-(A-)S-H equilibrated at 7-80 °C. The uncertainty of MCL (reproduced from [46]) is ± 1.25, except for the Al/Si* = 0.1 sample equilibrated at 80 °C, where the uncertainty of the MCL is represented by error bars. Al/Si* = 0.05 samples are marked as diamond and Al/Si* = 0.1 samples are marked as square. Al/Si* = bulk Al/Si.

3.3 Morphology of C-(A-)S-H

3.3.1 Effect of Ca/Si and Al inclusion at 20 °C

Ptychographic images of C-S-H (Ca/Si* = 1, equilibrated at 20 °C) show that this phase exhibits a crumpled foil-like morphology (Figure 8A). The foils at the fringe of the grain represent high length-to-width aspect ratio. The interior of the particle is a network of multiple densely-packed foils. We expect that the features in this image represent the nature of C-S-H under ambient pressure. Richardson and Groves [35] observed similar morphological features in water-activated slag/PC paste by TEM. The C-S-H outer product formed in β-dicalcium silicate (β-Ca_2SiO_4, β-C_2S), tricalcium silicate (Ca_3SiO_5,

444 C_3S), and PC pastes in studies using TEM [2, 23, 40] and ptychographic imaging [78]
445 present fibers with more linear directional features. This is possibly due to much higher
446 lime concentrations in the pore solutions of these materials and/or much greater space
447 constraints (much lower water-to-solid ratio).
448
449
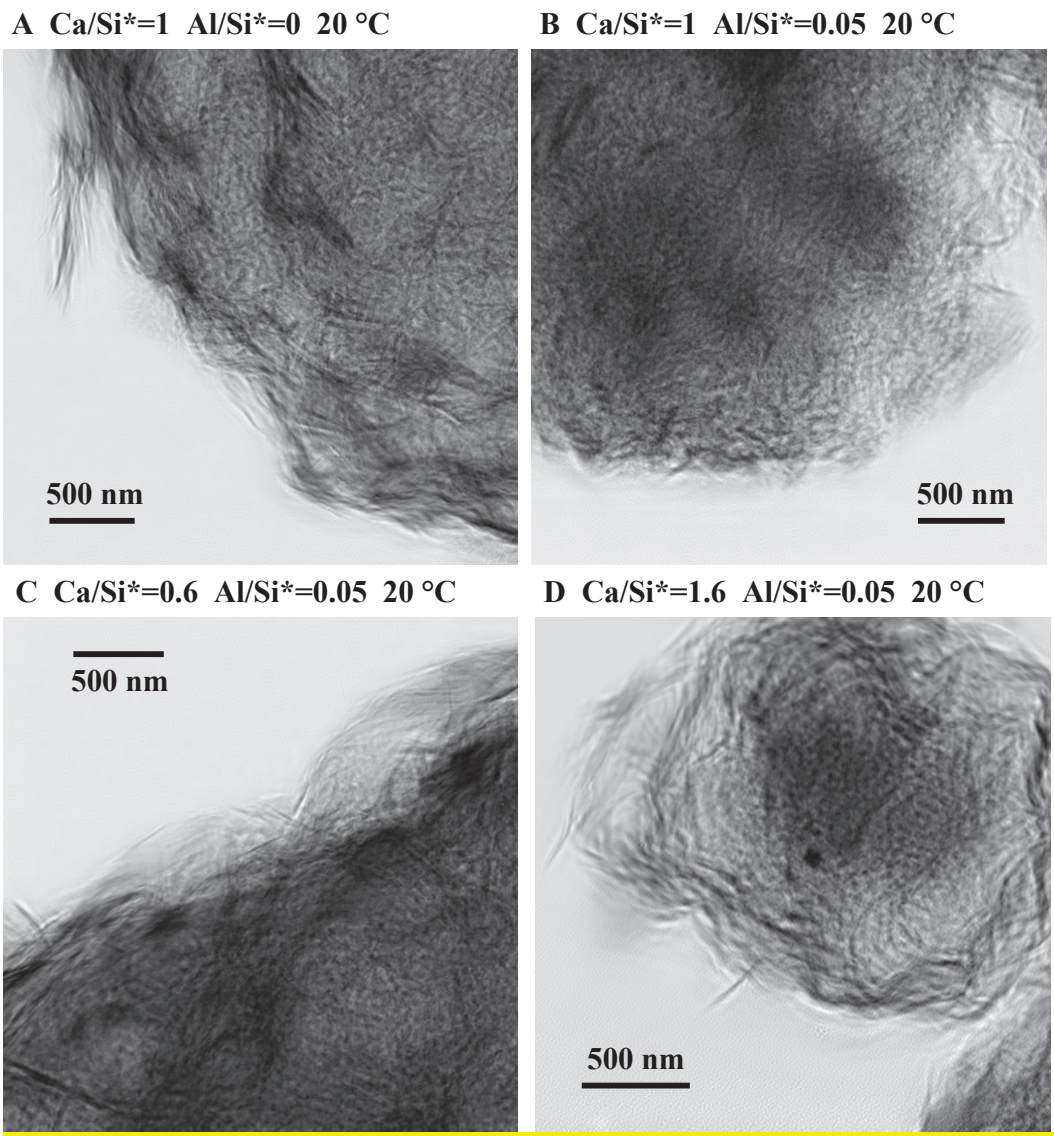

450
451 **Figure 8.** Ptychographic magnitude images of C-(A-)S-H equilibrated at 20 °C for 182
452 days: A) Ca/Si* = 1.0, Al/Si* = 0; B) Ca/Si* = 1.0, Al/Si* = 0.05; C) Ca/Si* = 0.6,
453 Al/Si* = 0.05; and D) Ca/Si = 1.6, Al/Si* = 0.05. Ca/Si* = bulk Ca/Si. Al/Si* = bulk
454 Al/Si.
455

A recent TEM study showed that the C-S-H precipitated at Ca/Si*=1 and using a similar water-to-solid ratio is also foil-like. The slight morphological difference of the C-S-H phase in that study relative to the present work can be attributed to different drying and vacuum conditions [79]. The morphology of C-S-H in hydrated C_3S in that study transitioned from foils to fibers as Ca concentration in solution increases [39].

A plateau (Figure S2, Supplementary Information) is observed in small angle scattering curve obtained from ptychographic image, suggesting the presence of concentrated packing of 'platelet' building blocks and strong polydispersion [78]. We calculated the average thickness of this C-S-H platelet based on a lamellar model to be ~7 nm (from ptychographic magnitude image); therefore the average number of layers of the C-S-H platelets in the *c*-direction is ~5.6. A TEM study shows that C-S-H equilibrated at 20 °C from $CaO\text{-}SiO_2\text{-}H_2O$ system is also foil-like at Ca/Si = 0.75-1.42, and the thickness of the foil is ~ 5-8 nm [39]. The distinction in thickness from the present work is expected due to different drying processes, vacuum conditions, and hydration ages.

Incorporation of Al into the C-A-S-H phase at 20 °C does not greatly alter its morphology, which is also identified as a network of crumpled foils. It appears similar to the outer product of water-activated slag hydrated for 3.5 years [2]. Variation in morphology of C-A-S-H (Al/Si* = 0.05, equilibrated at 20 °C) is not observed at Ca/Si* = 0.6, 1, 1.2, or 1.6 (Figure 8 and Figure S1 in Appendix B, Supplementary Information), suggesting that the Ca/Si ratio does not significantly govern the nano-morphology of C-A-S-H equilibrated at 20 °C. We calculate the average thickness of C-A-S-H platelets at

480 this temperature to be 5.9-7.3 nm (Appendix C, Supplementary Information), which does
481 not vary greatly as a function of the Ca/Si ratio, therefore the average number of layers of
482 the C-A-S-H platelets ranges from ~4.3 to ~5.9. TEM micrographs by Rodriguez et al.
483 [39] show that C-S-H synthesized in the CaO-SiO_2–H_2O system at 20 °C always appears
484 to be foil-like regardless of Ca/Si. The slight morphological difference between the two
485 studies can be attributed to the Al inclusion, drying process and other factors (e.g.,
486 vacuum condition and water-to-solid ratio).
487

488 **3.3.2 Effects of temperature and cross-linking**

489

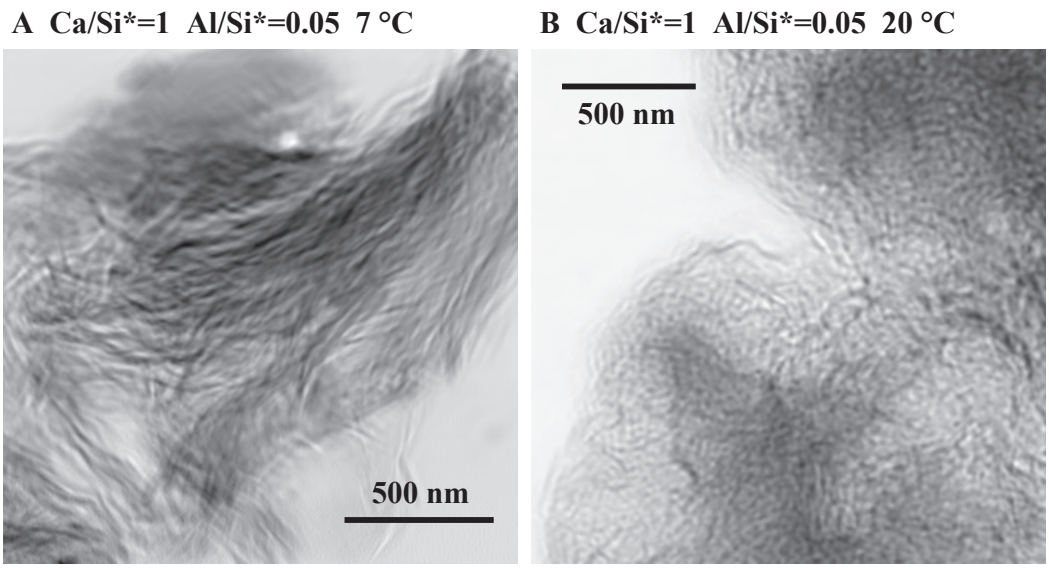

490

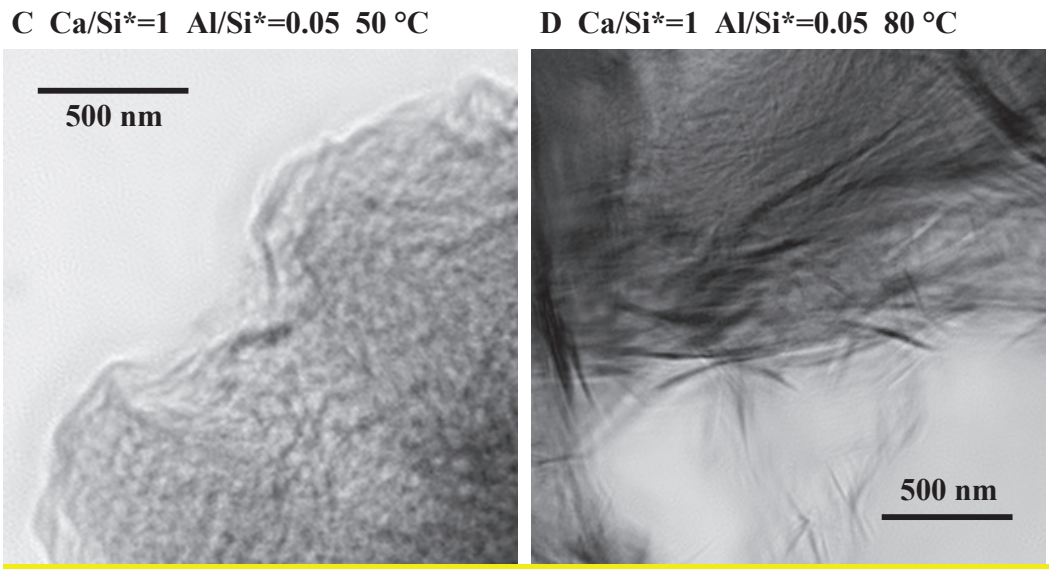

Figure 9. Ptychographic magnitude images of C-A-S-H with Ca/Si* = 1 and Al/Si* = 0.05; A) equilibrated for 365 days at 7 °C; B) equilibrated for 182 days at 20 °C; C) equilibrated for 56 days at 50°C; D) equilibrated for 56 days at 80°C.

The C-A-S-H phases (Ca/Si* = 1, Al/Si* = 0.05) precipitated using equilibration temperatures of 7 to 50 °C are morphologically similar (Figure 9), while the morphologies of C-A-S-H phases appear to be significantly different at 80 °C (Figure 10). The average thickness of C-A-S-H platelet is 5.3-6.5 nm for the 7-50 °C samples, while the average thickness of C-A-S-H for 80 °C samples is 14.5- 14.7 nm (Appendix C, Supplementary Information). Thus, the average number of stacked layers of the C-A-S-H platelets is ~4.8-5.3 for the 7-50 °C samples, while the average number of layers is 12.7-12.9 for the 80 °C samples. C-A-S-H samples with different Al/Si* ratios at 80 °C all present foil-predominant network, and the C-A-S-H at Al/Si* = 0.1 presents much thicker and wider agglomeration of foil structure than that at Al/Si* = 0.05. This observation shows that the Al incorporation at 80 °C significantly alters the morphology of C-(A-)S-H. This effect is likely related to the increased crystalline order of this sample, although it

508 may also be caused by its cross-linking of aluminosilicate chains and noticeably
509 increased degree of C-A-S-H chain polymerization.
510

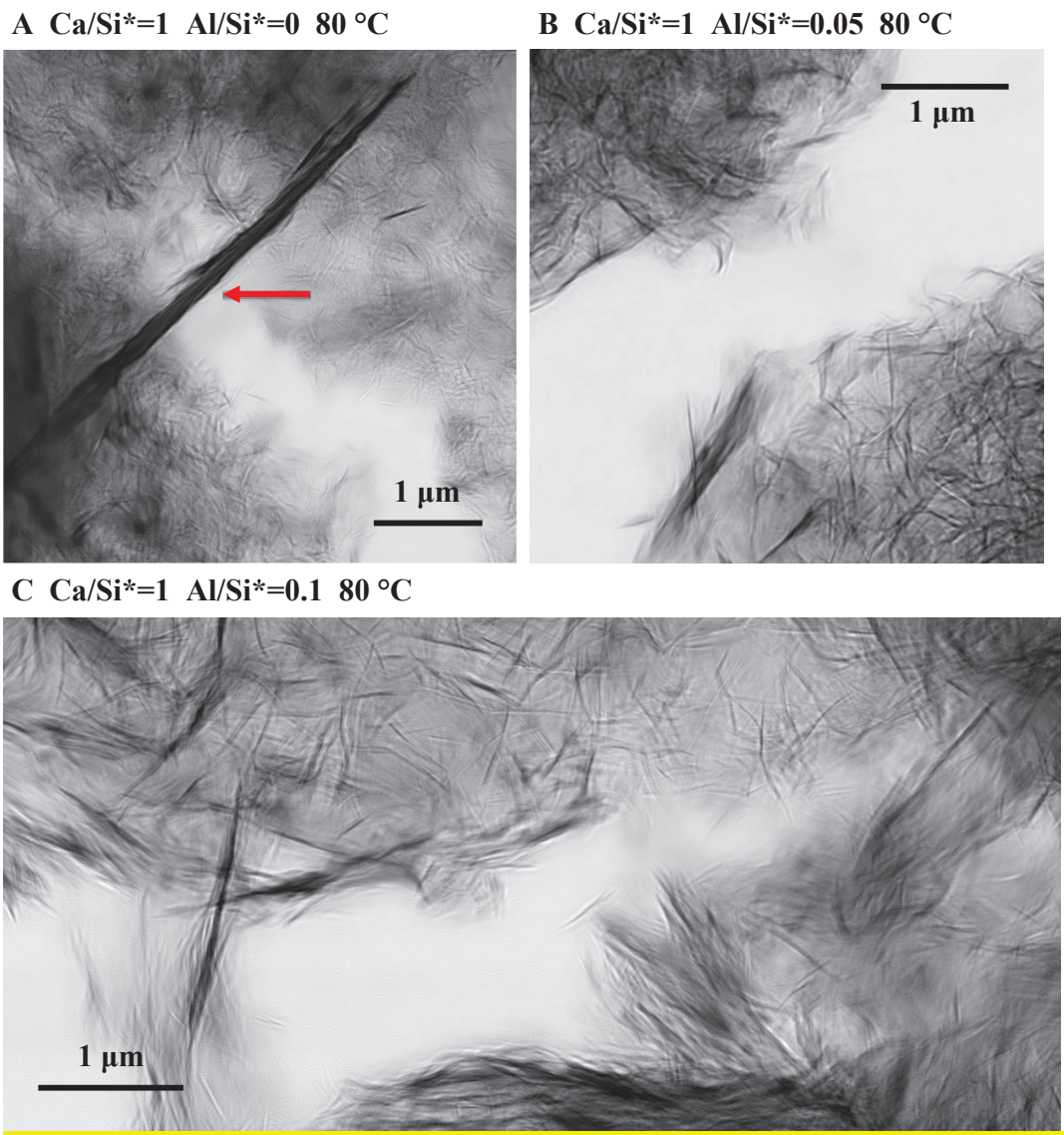

511
512
513 **Figure 10.** A) Ptychographic magnitude images of C-(A-)S-H equilibrated for 56 days at
514 80 °C: A) Ca/Si* = 1, Al/Si* = 0; B) Ca/Si* = 1, Al/Si* = 0.05; C) Ca/Si* = 1, Al/Si* =
515 0.1. Tobermorite crystal with an average basal spacing of 13.8 Å is indicated by a red
516 arrow. Ca/Si*= bulk Ca/Si. Al/Si*= bulk Al/Si.
517

For samples equilibrated at 80 °C, the C-S-H foils are thinner and shorter than the C-A-S-H foils (both samples have Ca/Si* = 1.0). However, these foils are coarser than the C-(A-)S-H foils equilibrated at 7-50 °C (Ca/Si* = 1.0); the average basal spacing of the foils equilibrated at 80 °C is 12.1 Å (WAXS results in Appendix A, Supplementary Information). SAS calculations confirm this significant change in morphology, which give an average stacked C-S-H platelet thickness for the 80 °C sample of 8.5 nm and an average number of layers of ~7. The coarse fibers with variable lengths ranging from hundreds of nanometers to a few microns in C-S-H at 80 °C correspond to a tobermorite-like structure with an average basal spacing of ~13.8 Å. The change in morphology in terms of elevated temperature is different from C-S-H gels in hydrated C_3S paste at 80 °C [23], which can be explained by the difference in the lime concentration of pore solution, space constraint and reaction kinetics.

3.4 A molecular-to-nanoscale model of C-A-S-H

A molecular-to-nanoscale model (Figure 11) of the hypothetical C-A-S-H structure at equilibration temperature of 7 to 80 °C is proposed based on the results of coordination environment, morphology, and model fitting of SAS in terms of the stacked layer-structure. C-A-S-H equilibrated at 7 - 50 °C is structurally analogous to defective tobermorite, which contains CaO_7 sheets flanked with "dreierketten" – tetrahedral aluminosilicate chains – on one side and counter-ions (highly distorted six-fold coordinated Ca and five-fold coordinated Al) and water in an interlayer on the other. In this temperature range, cross-linked sites do not exist and Al is preferably incorporated at bridging sites (Q^2_B) of the aluminosilicate chains. The basal spacing of C-A-S-H structure

541 varies from ~12 to 14 Å with varying Ca/Si ratios due to the Al-uptake and zeolitic
542 content (Ca ions and water). The stacked thickness of lamellar building blocks of C-A-S-
543 H at 7 - 50 °C ranges from 5.3 to 7.3 nm, representing ~4-6 stacked layers along the *c*-
544 axis. Therefore, the building blocks constitute a network of crumpled densely-packed
545 foils at the nanoscale.
546
547 Tedtrahedral-coordinated Al also substitutes into cross-linked sites (Q^3) of chains in C-A-
548 S-H equilibrated at 80 °C, which decreases the basal spacing to ~11.4 Å and significantly
549 increases the polymerization of aluminosilicate chains. The elevated equilibration
550 temperature does not alter the coordination symmetry of Ca species in C-A-S-H structure
551 but triggers a longer-range of ordering of CaO_7 sheets. The average thickness of C-A-S-H
552 building blocks at 80 °C is ~14.6 nm, denoting ~13 stacked layers along the *c*-axis. The
553 coarser C-A-S-H building blocks constitute a foil-predominant network with less
554 curvature and wider and thicker agglomeration at the nanoscale.
555

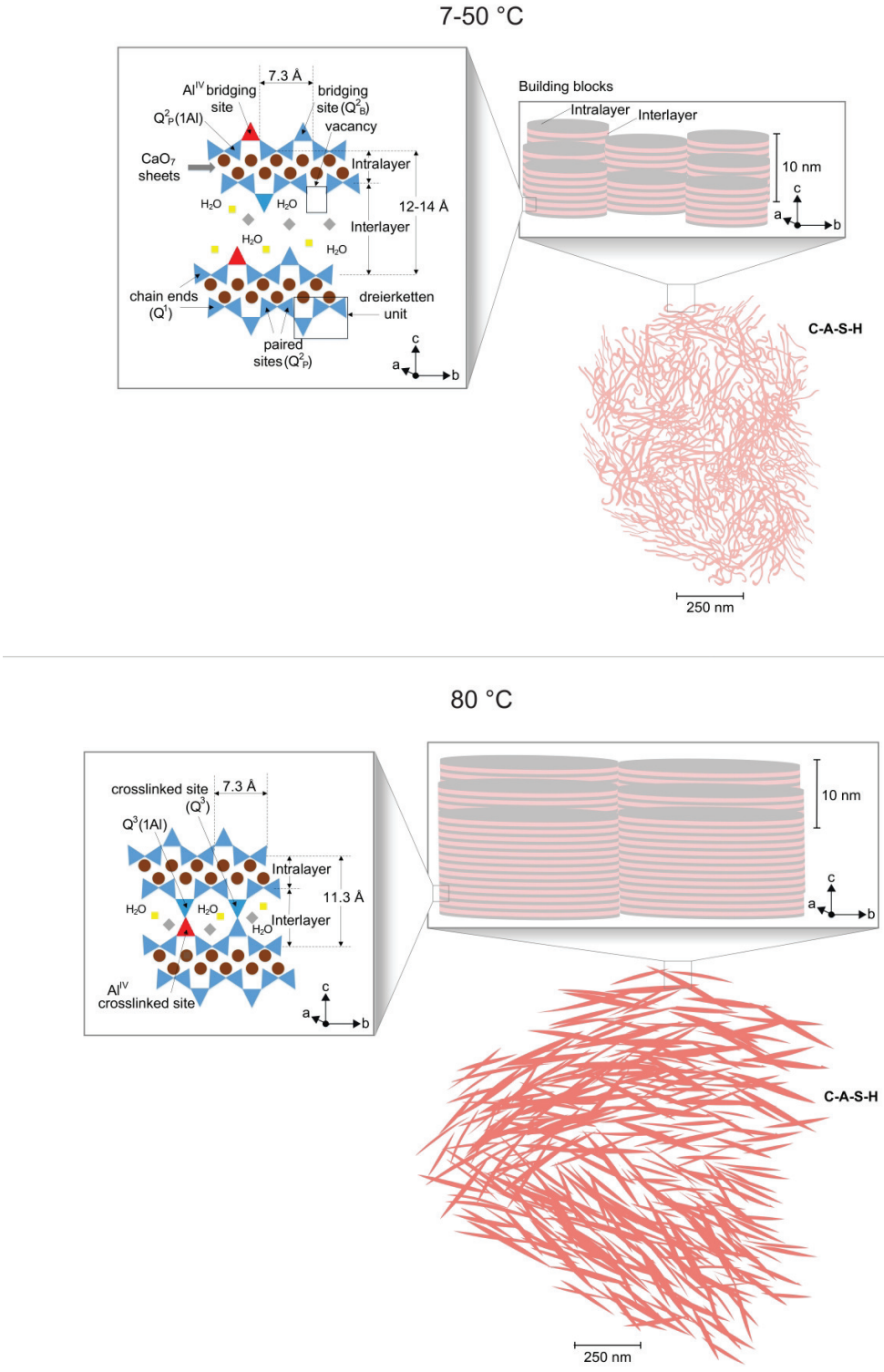

Figure 11. Schematic diagram of nanocrystalline C-A-S-H (equilibration temperature of 7 to 80°C). Brown circles represent Ca species in the CaO_7 sheets, and blue and red triangles denote SiO_4 and AlO_4 tetrahedron sites, respectively. The grey diamonds and

yellow squares are counterions (e.g., Ca species and five-fold coordinated Al species) in the interlayer. Pink and grey alternating stacked layers of the building blocks represent interlayer and intralayer, respectively. Rouge foils denote the networking structure of C-A-S-H at the nanoscale.

4. Conclusions

This paper has presented a synchrotron-based X-ray micro-spectroscopy study of C-(A-)S-H of different Ca/Si and Al/Si ratios, that were equilibrated at temperatures between 7 and 80 °C. The key conclusions are:

- Apart from the seven-fold coordinated Ca in the intralayer of C-(A-)S-H, the extra Ca that enters the interlayer are more likely six-fold coordinated in a distorted octahedral symmetry. The ordering of the Ca environment increases as Al content and equilibration temperature increase.
- Calcium environments in C-(A-)-S-H are similar to tobermorite. The coordination symmetry of Ca is highly distorted irrespective Ca/Si, Al uptake, and equilibration temperature.
- The Si *K*-edge shifts to higher energy with increased mean chain length of silicate chains. The energy separation between major and minor peak at the Si *K*-edge positively correlates with the degree of polymerization of its aluminosilicate chains.
- The Si-O bond length increases as the bulk Ca/Si ratio increases. Al incorporation leads to contraction of Si-O bonds in silicate tetrahedra in C-A-S-H.
- AFm-like species are not interstratified in the interlayer structure or precipitate on the external surface of C-A-S-H. TAH is either not Ca-bearing or its Ca is

structurally similar to C-(A-)S-H. Al is preferably incorporated at bridging sites and is also accommodated in cross-linked bridging sites at 80 °C.

- C-S-H at Ca/Si*=1 formed at 20°C preferably presents crumpled foils with various lengths. The Al-uptake of C-S-H at 7-50 °C and Ca/Si ratio do not change its morphology. C-A-S-H equilibrated at 80 °C present coarser foils, and the foils are much thicker and longer with more Al inclusion.
- The building-block of all C-(A-)S-H samples is lamellar. C-A-S-H is morphologically similar with comparable lamellar thickness irrespective of Ca/Si or equilibration temperature at 7-50 °C. The lamellar thickness of C-S-H equilibrated at 80 °C is slightly enhanced, and the thickness is much greater with Al inclusion.

These results provide new insight into the morphology of C-(A-)S-H and the possible nature of TAH in C-A-S-H products, the coordination of Ca-O, and the environment of Si in C-(A-)S-H with different compositions and synthesized at different equilibration temperatures. Therefore, this paper yields an improved understanding of C-(A-)S-H chemistry, which will enhance the understanding of the performance of hydrated PC blends in service.

Acknowledgements

The authors thank Barbara Lothenbach for providing the C-(A-)S-H samples that were synthesized by Rupert J. Myers and Emilie L'Hôpital at the Laboratory for Concrete & Construction Chemistry (EMPA), Juan F.C. Vinasco for assistance with the STXM

experiments, Sinem Ortaboy for helpful suggestions, and Tamika Bassman and Chen Li for the collaboration during the designing of Figures. This research is funded by the US National Science Foundation under the SusChEM Program, grant #DMR-1410557. This work is further supported by the Republic of Singapore's National Research Foundation through a grant to the Berkeley Education Alliance for Research in Singapore (BEARS) for the Singapore-Berkeley Building Efficiency and Sustainability in the Tropics (SinBerBEST) Program. The Advanced Light Source is supported by the Director, Office of Science, Office of Basic Energy Sciences, of the U.S. Department of Energy under Contract No. DE-AC02-05CH11231.

References

1. Monteiro, P.J., S.A. Miller and A. Horvath, *Towards sustainable concrete.* Nature materials, 2017. **16**(7): p. 698.
2. Richardson, I.G., *The nature of C-S-H in hardened cements.* Cement and Concrete Research, 1999. **29**(8): p. 1131-1147.
3. Li, C., H. Zhu, M. Wu, K. Wu and Z. Jiang, *Pozzolanic reaction of fly ash modified by fluidized bed reactor-vapor deposition.* Cement and Concrete Research, 2017. **92**: p. 98-109.
4. Li, C., M. Wu, Q. Chen and Z. Jiang, *Chemical and mineralogical alterations of concrete subjected to chemical attacks in complex underground tunnel environments during 20–36 years.* Cement and Concrete Composites, 2018. **86**: p. 139-159.
5. Bonaccorsi, E., S. Merlino and A.R. Kampf, *The crystal structure of tobermorite 14 A (Plombierite), a C-S-H phase.* Journal of the American Ceramic Society, 2005. **88**(3): p. 505-512.
6. Merlino, S., E. Bonaccorsi and T. Armbruster, *The real structure of tobermorite 11 angstrom: normal and anomalous forms, OD character and polytypic modifications.* European Journal of Mineralogy, 2001. **13**(3): p. 577-590.
7. Merlino, S., E. Bonaccorsi and T. Armbruster, *The real structures of clinotobermorite and tobermorite 9 angstrom: OD character, polytypes, and*

structural relationships. European Journal of Mineralogy, 2000. **12**(2): p. 411-429.
8. Merlino, S., E. Bonaccorsi and A.R. Kampf, *Tobermorite 14 angstrom: Crystal structure and OD character.* Applied Mineralogy, Vols 1 and 2, 2000: p. 859-861.
9. Merlino, S., E. Bonaccorsi and T. Armbruster, *Tobermorites: Their real structure and order-disorder (OD) character.* American Mineralogist, 1999. **84**(10): p. 1613-1621.
10. Ortaboy, S., J. Li, G. Geng, R.J. Myers, P.J. Monteiro, R. Maboudian and C. Carraro, *Effects of CO 2 and temperature on the structure and chemistry of C–(A–) S–H investigated by Raman spectroscopy.* RSC Advances, 2017. **7**(77): p. 48925-48933.
11. Renaudin, G., J. Russias, F. Leroux, C. Cau-dit-Coumes and F. Frizon, *Structural characterization of C–S–H and C–A–S–H samples—Part II: Local environment investigated by spectroscopic analyses.* Journal of Solid State Chemistry, 2009. **182**(12): p. 3320-3329.
12. Pardal, X., F. Brunet, T. Charpentier, I. Pochard and A. Nonat, *27Al and 29Si solid-state NMR characterization of calcium-aluminosilicate-hydrate.* Inorganic chemistry, 2012. **51**(3): p. 1827-1836.
13. Sun, G., J.F. Young and R.J. Kirkpatrick, *The role of Al in C–S–H: NMR, XRD, and compositional results for precipitated samples.* Cement and Concrete Research, 2006. **36**(1): p. 18-29.
14. L'Hôpital, E., B. Lothenbach, G. Le Saout, D. Kulik and K. Scrivener, *Incorporation of aluminium in calcium-silicate-hydrates.* Cement and Concrete Research, 2015. **75**: p. 91-103.
15. Faucon, P., A. Delagrave, J. Petit, C. Richet, J. Marchand and H. Zanni, *Aluminum incorporation in calcium silicate hydrates (CSH) depending on their Ca/Si ratio.* The Journal of Physical Chemistry B, 1999. **103**(37): p. 7796-7802.
16. Pardal, X., I. Pochard and A. Nonat, *Experimental study of Si–Al substitution in calcium-silicate-hydrate (CSH) prepared under equilibrium conditions.* Cement and Concrete Research, 2009. **39**(8): p. 637-643.
17. Brough, A. and A. Atkinson, *Sodium silicate-based, alkali-activated slag mortars: Part I. Strength, hydration and microstructure.* Cement and Concrete Research, 2002. **32**(6): p. 865-879.
18. Myers, R.J., S.A. Bernal, R. San Nicolas and J.L. Provis, *Generalized structural description of calcium–sodium aluminosilicate hydrate gels: the cross-linked substituted tobermorite model.* Langmuir, 2013. **29**(17): p. 5294-5306.
19. Myers, R.J., S.A. Bernal, J.D. Gehman, J.S. Deventer and J.L. Provis, *The Role of Al in Cross-Linking of Alkali-Activated Slag Cements.* Journal of the American Ceramic Society, 2015. **98**(3): p. 996-1004.
20. Vollpracht, A., B. Lothenbach, R. Snellings and J. Haufe, *The pore solution of blended cements: a review.* Materials and Structures, 2016. **49**(8): p. 3341-3367.

21. Hamid, S., *The crystal structure of the 11 Ä natural tobermorite Ca2. 25 [Si3O7. 5 (OH) 1.5]· 1H2O.* Zeitschrift für Kristallographie-Crystalline Materials, 1981. **154**(1-4): p. 189-198.
22. Grutzeck, M.W., *A new model for the formation of calcium silicate hydrate (C-S-H).* Materials Research Innovations, 1999. **3**(3): p. 160-170.
23. Richardson, I.G., *Tobermorite/jennite- and tobermorite/calcium hydroxide-based models for the structure of C-S-H: applicability to hardened pastes of tricalcium silicate, beta-dicalcium silicate, Portland cement, and blends of Portland cement with blast-fumace slag, metakaolin, or silica fume.* Cement and Concrete Research, 2004. **34**(9): p. 1733-1777.
24. Zhou, Y., D. Hou, J. Jiang, W. She and J. Li, *Molecular dynamics study on the solvated aniline (AN) and ethylene glycol (EG) monomers confined in calcium silicate nanometer channel: a case study of Tobermorite.* Physical Chemistry Chemical Physics, 2017.
25. Pellenq, R.J.-M., A. Kushima, R. Shahsavari, K.J. Van Vliet, M.J. Buehler, S. Yip and F.-J. Ulm, *A realistic molecular model of cement hydrates.* Proceedings of the National Academy of Sciences, 2009. **106**(38): p. 16102-16107.
26. Lequeux, N., A. Morau, S. Philippot and P. Boch, *Extended X-ray absorption fine structure investigation of calcium silicate hydrates.* Journal of the American Ceramic Society, 1999. **82**(5): p. 1299-1306.
27. Biagioni, C., S. Merlino and E. Bonaccorsi, *The tobermorite supergroup: a new nomenclature.* Mineralogical Magazine, 2015. **79**(2): p. 485-495.
28. Biagioni, C., E. Bonaccorsi, S. Merlino and D. Bersani, *New data on the thermal behavior of 14 angstrom tobermorite.* Cement and Concrete Research, 2013. **49**: p. 48-54.
29. Merlino, S., E. Bonaccorsi, M. Merlini, F. Marchetti and W. Garra, *Tobermorite 11 angstrom and its synthetic counterparts: Structural relationships and thermal behaviour.* Minerals as Advanced Materials I, 2008: p. 37-44.
30. Bonaccorsi, E. and S. Merlino, *Crystal chemistry and structural arrangements of 'normal' and 'anomalous' tobermorite 11 angstrom.* Applied Mineralogy, Vols 1 and 2, 2000: p. 735-738.
31. Kirkpatrick, R.J., G.E. Brown, N. Xu and X.D. Cong, *Ca X-ray absorption spectroscopy of C-S-H and some model compounds.* Advances in Cement Research, 1997. **9**(33): p. 31-36.
32. Soyer-Uzun, S., S.R. Chae, C.J. Benmore, H.R. Wenk and P.J.M. Monteiro, *Compositional Evolution of Calcium Silicate Hydrate (C-S-H) Structures by Total X-Ray Scattering.* Journal of the American Ceramic Society, 2012. **95**(2): p. 793-798.
33. Moudrakovski, I.L., R. Alizadeh and J.J. Beaudoin, *Natural abundance high field 43Ca solid state NMR in cement science.* Physical Chemistry Chemical Physics, 2010. **12**(26): p. 6961-6969.
34. Richardson, I.G., *Model structures for C-(A)-SH (I).* Acta Crystallographica Section B: Structural Science, Crystal Engineering and Materials, 2014. **70**(6): p. 903-923.

35. Richardson, I.G. and G.W. Groves, *Microstructure and Microanalysis of Hardened Cement Pastes Involving Ground Granulated Blast-Furnace Slag.* Journal of Materials Science, 1992. **27**(22): p. 6204-6212.
36. Taylor, R., I.G. Richardson and R.M.D. Brydson, *Composition and microstructure of 20-year-old ordinary Portland cement-ground granulated blast-furnace slag blends containing 0 to 100% slag.* Cement and Concrete Research, 2010. **40**(7): p. 971-983.
37. Richardson, I.G., *The calcium silicate hydrates.* Cement and Concrete Research, 2008. **38**(2): p. 137-158.
38. Richardson, I.G., *The nature of the hydration products in hardened cement pastes.* Cement & Concrete Composites, 2000. **22**(2): p. 97-113.
39. Rodriguez, E.T., I.G. Richardson, L. Black, E. Boehm-Courjault, A. Nonat and J. Skibsted, *Composition, silicate anion structure and morphology of calcium silicate hydrates (C-S-H) synthesised by silica-lime reaction and by controlled hydration of tricalcium silicate (C3S).* Advances in Applied Ceramics, 2015. **114**(7): p. 362-371.
40. Richardson, I.G. and G.W. Groves, *Microstructure and Microanalysis of Hardened Ordinary Portland-Cement Pastes.* Journal of Materials Science, 1993. **28**(1): p. 265-277.
41. Geng, G., J. Li, Y.-S. Yu, D.A. Shapiro, D.A. Kilcoyne and P.J. Monteiro, *Nanometer-Resolved Spectroscopic Study Reveals the Conversion Mechanism of CaO· Al2O3· 10H2O to 2CaO· Al2O3· 8H2O and 3CaO· Al2O3· 6H2O at an Elevated Temperature.* Crystal Growth & Design, 2017. **17**(8): p. 4246-4253.
42. da Silva, J.C., P. Trtik, A. Diaz, M. Holler, M. Guizar-Sicairos, J.r. Raabe, O. Bunk and A. Menzel, *Mass density and water content of saturated never-dried calcium silicate hydrates.* Langmuir, 2015. **31**(13): p. 3779-3783.
43. Geng, G.Q., R. Taylor, S. Bae, D. Hernandez-Cruz, D.A. Kilcoyne, A.H. Emwas and P.J.M. Monteiro, *Atomic and nano-scale characterization of a 50-year-old hydrated C3S paste.* Cement and Concrete Research, 2015. **77**: p. 36-46.
44. Li, Q.G., Y.; Geng, G.; Bae, S.; Monteiro, P. J. M.;, *CaCl2-Accelerated Hydration of Tricalcium Silicate: A STXM Study Combined with 29Si MAS NMR.* Journal of Nanomaterials, 2015. **2015**: p. 1-10.
45. Bae, S., R. Taylor, D. Hernandez-Cruz, S. Yoon, D. Kilcoyne and P.J.M. Monteiro, *Soft X-ray Spectromicroscopic Investigation of Synthetic C-S-H and C3S Hydration Products.* Journal of the American Ceramic Society, 2015. **98**(9): p. 2914-2920.
46. Myers, R.J., E. L'Hopital, J.L. Provis and B. Lothenbach, *Effect of temperature and aluminium on calcium (alumino)silicate hydrate chemistry under equilibrium conditions.* Cement and Concrete Research, 2015. **68**: p. 83-93.
47. Kilcoyne, A.L.D., T. Tyliszczak, W.F. Steele, S. Fakra, P. Hitchcock, K. Franck, E. Anderson, B. Harteneck, E.G. Rightor, G.E. Mitchell, A.P. Hitchcock, L. Yang, T. Warwick and H. Ade, *Interferometer-controlled scanning transmission X-ray microscopes at the Advanced Light Source.* Journal of Synchrotron Radiation, 2003. **10**: p. 125-136.

48. Kilcoyne, D., et al., *A new scanning transmission X-ray Microscope at the ALS for operation up to 2500 eV.* AIP Conference Proceedings, 2010: p. 465.
49. Naftel, S.J., T.K. Sham, Y.M. Yiu and B.W. Yates, *Calcium L-edge XANES study of some calcium compounds.* Journal of Synchrotron Radiation, 2001. **8**: p. 255-257.
50. Ko, J.P., *X-ray Absorption Near-edge Structure (XANES) of Calcium L~ 3~,~ 2 Edges of Various Calcium Compounds and X-ray Excited Optical Luminescence (XEOL) Studies of Luminescent Calcium Compounds.* X-Ray Absorption Fine Structure--XAFS, 2007. **13**(882): p. 538-540.
51. Degroot, F.M.F., J.C. Fuggle, B.T. Thole and G.A. Sawatzky, *2p X-Ray Absorption of 3d Transition-Metal Compounds - an Atomic Multiplet Description Including the Crystal-Field.* Physical Review B, 1990. **42**(9): p. 5459-5468.
52. Geng, G., R.J. Myers, A.L. Kilcoyne, J. Ha and P.J. Monteiro, *Ca L2, 3-edge near edge X-ray absorption fine structure of tricalcium aluminate, gypsum, and calcium (sulfo) aluminate hydrates.* American Mineralogist, 2017. **102**(4): p. 900-908.
53. Fleet, M.E. and X.Y. Liu, *Calcium L-2,L-3-edge XANES of carbonates, carbonate apatite, and oldhamite (CaS).* American Mineralogist, 2009. **94**(8-9): p. 1235-1241.
54. Hanhan, S., A.M. Smith, M. Obst and A.P. Hitchcock, *Optimization of analysis of soft X-ray spectromicroscopy at the Ca 2p edge.* Journal of Electron Spectroscopy and Related Phenomena, 2009. **173**(1): p. 44-49.
55. L'Hôpital, E., B. Lothenbach, K. Scrivener and D. Kulik, *Alkali uptake in calcium alumina silicate hydrate (CASH).* Cement and Concrete Research, 2016. **85**: p. 122-136.
56. L'Hôpital, E., B. Lothenbach, D. Kulik and K. Scrivener, *Influence of calcium to silica ratio on aluminium uptake in calcium silicate hydrate.* Cement and Concrete Research, 2016. **85**: p. 111-121.
57. Walker, C.S., D. Savage, M. Tyrer and K.V. Ragnarsdottir, *Non-ideal solid solution aqueous solution modeling of synthetic calcium silicate hydrate.* Cement and Concrete Research, 2007. **37**(4): p. 502-511.
58. Geng, G.Q., R.J. Myers, M.J.A. Qomi and P.J.M. Monteiro, *Densification of the interlayer spacing governs the nanomechanical properties of calcium-silicate-hydrate.* Scientific Reports, 2017. **7**.
59. Gartner, E., I. Maruyama and J. Chen, *A new model for the CSH phase formed during the hydration of Portland cements.* Cement and Concrete Research, 2017. **97**: p. 95-106.
60. Black, L., K. Garbev, G. Beuchle, P. Stemmermann and D. Schild, *X-ray photoelectron spectroscopic investigation of nanocrystalline calcium silicate hydrates synthesised by reactive milling.* Cement and Concrete Research, 2006. **36**(6): p. 1023-1031.
61. Renaudin, G., J. Russias, F. Leroux, F. Frizon and C. Cau-dit-Coumes, *Structural characterization of C–S–H and C–A–S–H samples—part I: long-range order investigated by Rietveld analyses.* Journal of Solid State Chemistry, 2009. **182**(12): p. 3312-3319.

62. Andersen, M.D., H.J. Jakobsen and J. Skibsted, *A new aluminium-hydrate species in hydrated Portland cements characterized by 27 Al and 29 Si MAS NMR spectroscopy.* Cement and Concrete Research, 2006. **36**(1): p. 3-17.
63. Li, D., G.M. Bancroft, M.E. Fleet and X.H. Feng, *Silicon K-Edge Xanes Spectra of Silicate Minerals.* Physics and Chemistry of Minerals, 1995. **22**(2): p. 115-122.
64. Cabaret, D., M. Le Grand, A. Ramos, A.M. Flank, S. Rossano, L. Galoisy, G. Calas and D. Ghaleb, *Medium range structure of borosilicate glasses from Si K-edge XANES: a combined approach based on multiple scattering and molecular dynamics calculations.* Journal of Non-Crystalline Solids, 2001. **289**(1-3): p. 1-8.
65. Li, D., *Aluminum, Silicon, Phosphorus And Sulfur K-And L-edge X-ray Absorption Spectroscopy Of Minerals And Glasses: Applications In Mineralogy And Geochemistry.* PhD thesis,, 1994: p. 2432.
66. Henderson, G.S. and M.E. Fleet, *The structure of titanium silicate glasses investigated by Si K-edge X-ray absorption spectroscopy.* Journal of Non-Crystalline Solids, 1997. **211**(3): p. 214-221.
67. Bianconi, A., M. Dellariccia, P.J. Durham and J.B. Pendry, *Multiple-Scattering Resonances and Structural Effects in the X-Ray-Absorption near-Edge Spectra of Fe-Ii and Fe-Iii Hexacyanide Complexes.* Physical Review B, 1982. **26**(12): p. 6502-6508.
68. Bunker, G., *Introduction to XAFS: a practical guide to X-ray absorption fine structure spectroscopy.* Cambridge University Press, 2010.
69. Smith, K.A., R.J. Kirkpatrick, E. Oldfield and D.M. Henderson, *High-resolution silicon-29 nuclear magnetic resonance spectroscopic study of rock-forming silicates.* American Mineralogist, 1983. **68**(11-12): p. 1206-1215.
70. Hill, R. and G. Gibbs, *Variation in d (TO), d (T··· T) and∠ TOT in silica and silicate minerals, phosphates and aluminates.* Acta Crystallographica Section B: Structural Crystallography and Crystal Chemistry, 1979. **35**(1): p. 25-30.
71. Henderson, G.S., *A Si K-Edge Exafs/Xanes Study of Sodium-Silicate Glasses.* Journal of Non-Crystalline Solids, 1995. **183**(1-2): p. 43-50.
72. Yu, P., R.J. Kirkpatrick, B. Poe, P.F. McMillan and X.D. Cong, *Structure of calcium silicate hydrate (C-S-H): Near-, mid-, and far-infrared spectroscopy.* Journal of the American Ceramic Society, 1999. **82**(3): p. 742-748.
73. Garbev, K., P. Stemmermann, L. Black, C. Breen, J. Yarwood and B. Gasharova, *Structural features of C-S-H(I) and its carbonation in air - A Raman spectroscopic study. Part I: Fresh phases.* Journal of the American Ceramic Society, 2007. **90**(3): p. 900-907.
74. Black, L., K. Garbev, P. Stemmermann, K.R. Hallam and G.C. Allen, *Characterisation of crystalline C-S-H phases by X-ray photoelectron spectroscopy.* Cement and Concrete Research, 2003. **33**(6): p. 899-911.
75. Li, D., G.M. Bancroft, M. Kasrai, M.E. Fleet, X.H. Feng, K.H. Tan and B.X. Yang, *High-Resolution Si K-Edge and L2,3-Edge Xanes of Alpha-Quartz and Stishovite.* Solid State Communications, 1993. **87**(7): p. 613-617.
76. Li, D., G.M. Bancroft, M. Kasrai, M.E. Fleet, R.A. Secco, X.H. Feng, K.H. Tan and B.X. Yang, *X-Ray-Absorption Spectroscopy of Silicon Dioxide (Sio2)*

Polymorphs - the Structural Characterization of Opal. American Mineralogist, 1994. **79**(7-8): p. 622-632.
77. Geng, G., R.J. Myers, J. Li, R. Maboudian, C. Carraro, D.A. Shapiro and P.J. Monteiro, *Aluminum-induced dreierketten chain cross-links increase the mechanical properties of nanocrystalline calcium aluminosilicate hydrate.* Scientific Reports, 2017. **7**: p. 44032.
78. Bae, S., R. Taylor, D. Shapiro, P. Denes, J. Joseph, R. Celestre, S. Marchesini, H. Padmore, T. Tyliszczak and T. Warwick, *Soft X-ray Ptychographic Imaging and Morphological Quantification of Calcium Silicate Hydrates (C–S–H).* Journal of the American Ceramic Society, 2015. **98**(12): p. 4090-4095.
79. Fonseca, P. and H.M. Jennings, *The effect of drying on early-age morphology of C–S–H as observed in environmental SEM.* Cement and Concrete Research, 2010. **40**(12): p. 1673-1680.

Table 1. Features in the Ca $L_{2,3}$-edge XANES spectra of C-(A-)S-H samples. The estimated absolute errors are ± 0.01 eV in energy positions and ± 0.0002 units in intensity ratios.

Al/Si*	Ca/Si*	Energy (eV)								
		a_0	a_1	a_2	a_1/a_2	ΔL_3	b_1	b_2	b_1/b_2	ΔL_2
Equilibrium at 20°C										
0	0.6	347	348.0	349.1	0.0648	1.1	351.4	352.5	0.0944	1.1
	0.8	346.8	348.0	349.1	0.0618	1.1	351.35	352.45	0.0647	1.1
	1.0	348.8	348.0	349.1	0.0495	1.1	351.4	352.5	0.0756	1.1
	1.2	346.8	348.05	349.1	0.089	1.05	351.4	352.5	0.089	1.1
	1.4	346.8	347.95	349.0	0.0695	1.05	351.3	352.4	0.0935	1.1
	1.6	346.8	347.95	349.05	0.0842	1.1	351.25	352.4	0.1015	1.15
0.05	0.6	346.7	348.0	349.1	0.0992	1.1	351.4	352.5	0.1278	1.1
	0.8	346.8	348.0	349.1	0.0794	1.1	351.4	352.5	0.1382	1.1
	1.0	346.8	348.05	349.1	0.0798	1.05	351.45	352.5	0.1334	1.05
	1.2	346.8	348.0	349.1	0.144	1.1	351.4	352.5	0.1159	1.1
	1.4	346.8	348.0	349.1	0.0902	1.1	351.35	352.45	0.1501	1.1
	1.6	346.8	348.05	349.1	0.155	1.05	351.35	352.45	0.1482	1.1
Equilibrium at 7°C										
0	1.0	347*	348.0*	349.1	-	1.1	351.4	352.5	0.017	1.1
0.05	1.0	347*	348.0*	349.1	0.0134	1.1	351.4	352.5	0.053	1.1
0.1	1.0	346.8*	348.0*	349.1	0.0433	1.1	351.4	352.5	0.0856	1.1
Equilibrium at 50°C										
0	1.0	346.8	348.0	349.1	0.0814	1.1	351.35	352.5	0.0931	1.15
0.05	1.0	346.8	348.0	349.1	0.1188	1.1	351.4	352.5	0.1581	1.1
0.1	1.0	346.8	348.0	349.1	0.1303	1.1	351.4	352.5	0.171	1.1
Equilibrium at 80°C										
0	1.0	346.8	348.0	349.1	0.0861	1.1	351.4	352.5	0.1688	1.1
0.05	1.0	346.8	348.0	349.1	0.1458	1.1	351.4	352.5	0.2241	1.1
0.1	1.0	346.8	348.0	349.1	0.1718	1.1	351.4	352.5	0.2557	1.1

*weak peak, peak position is not clearly identified.

Table 2. Peak positions and energy differences of Si *K*-edge XANES spectra of C-(A-)S-H equilibrated at 20 °C. The estimated absolute errors are ± 0.05 units in positions of peak a_1 and at Ca/Si = 0.6-1.2, ± 0.1 units in position of peak a_1 at Ca/Si = 1.4- 1.6, and ± 0.15 units in position of peak a_2 and energy differences between peaks a_1 and a_2.

Ca/Si*	Peak a_1 (eV)	Peak a_2 (eV)	Δa_2-a_1 (eV)
Al/Si*=0			
0.6	1849.7	1866.6	16.9
0.8	1849.4	1865.6	16.2
1.0	1849.2	1865.1	15.9
1.2	1849.1	1864.8	15.7
1.4	1848.8	1864.6	15.4
1.6	1848.7	1864.0	15.3
Al/Si*=0.05			
0.6	1849.8	1866.9	17.1
0.8	1849.5	1865.9	16.4
1.0	1849.3	1865.4	16.1
1.2	1849.2	1865.1	15.9
1.4	1849.0	1864.8	15.8
1.6	1849.0	1864.6	15.6

Table 3. Features of Si *K*-edge XANES spectra for C-(A-)S-H samples (Ca/Si* = 1) equilibrated at different temperatures. The estimated absolute errors are ± 0.05 units in positions of peak a_1 for C-(A-)S-H equilibrated at 7 °C - 50 °C, ± 0.1 units in position of peak a_1 at for C-(A-)S-H equilibrated at 80 °C, and ± 0.15 units in position of peak a_2 and energy differences between peaks a_1 and a_2.

Al/Si*	Peak a_1 (eV)	Peak a_2 (eV)	Δa_2-a_1 (eV)
Equilibrium at 7°C			
0	1849.4	1865.3	15.9
0.05	1849.6	1865.6	16.0
0.1	1850.0	1866.2	16.2
Equilibrium at 20°C			
0	1849.2	1865.1	15.9
0.05	1849.3	1865.4	16.1
Equilibrium at 50°C			
0	1849.3	1865.1	15.8
0.05	1849.6	1865.7	16.1
0.1	1849.9	1866.1	16.2
Equilibrium at 80°C			
0 (12.1 Å)	1849.6	1865.6	16.0
0 (13.8 Å)	1849.7	1865.8	16.1
0.05	1850.2	1866.5	16.3
0.1	1850.4	1866.9	16.5

The basal spacing shown in parentheses was measured by wide-angle X-ray scattering (WAXS, Appendix A in Supplementary Information). Al/Si* = bulk Al/Si.

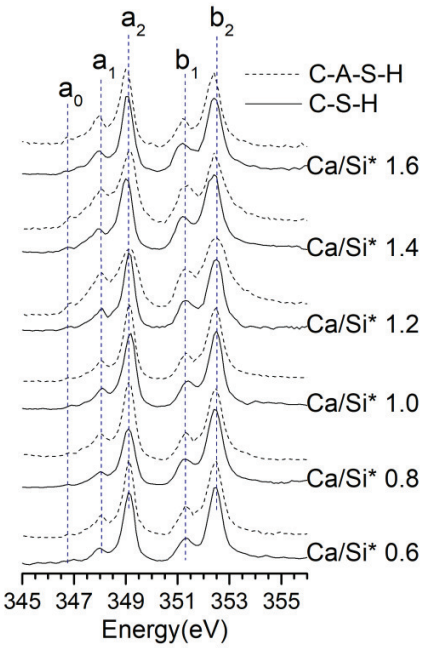

Figure 1. Ca $L_{2,3}$-edge XANES spectra of C-S-H (solid lines) and C-A-S-H with Al/Si* = 0.05 (dashed lines) after 182 days of hydration at 20 °C. Ca/Si* = bulk Ca/Si

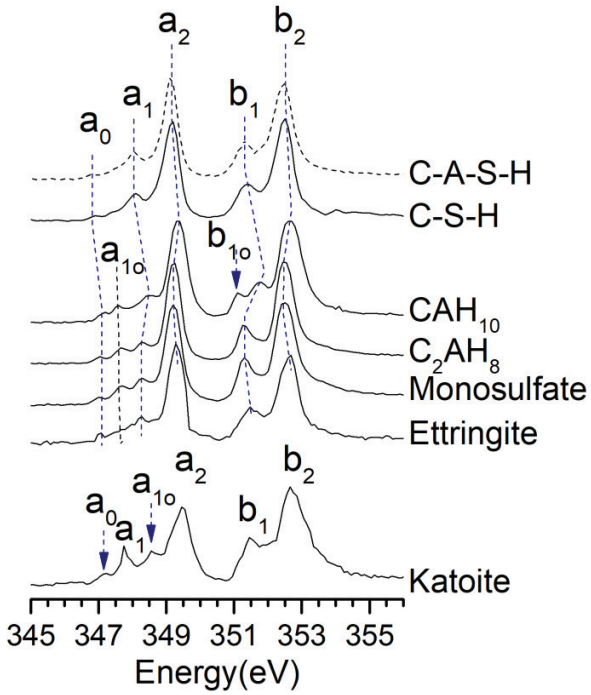

Figure 2. Ca $L_{2,3}$-edge XANES spectra of C-S-H (solid lines) and C-A-S-H (dashed lines, Al/Si* = 0.05) after 182 days of hydration at 20°C. Spectra of CAH_{10}, C_2AH_8, monosulfoaluminate (monosulfate, $C_4A\overline{S}H_{12}$), ettringite ($C_6A\overline{S}_3H_{32}$) and katoite (C_3AH_6) are taken from [41]. Ca/Si* = bulk Ca/Si.

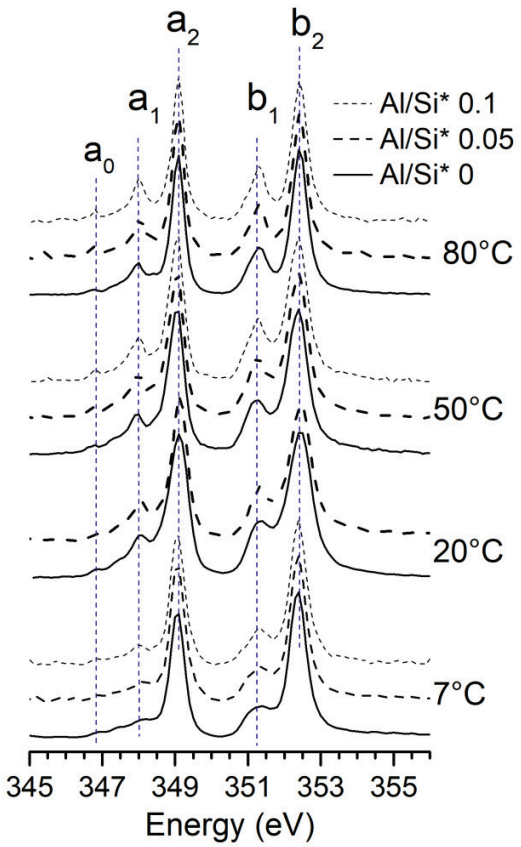

Figure 3. Ca $L_{2,3}$-edge XANES spectra of C-S-H (solid lines, Al/Si* = 0, Ca/Si* = 1.0), C-A-S-H (long-dashed lines, Al/Si* = 0.05, Ca/Si* = 1.0), and C-A-S-H (short-dashed lines, Al/Si* = 0.1, Ca/Si* = 1.0) at different equilibration temperatures. Ca/Si* = bulk Ca/Si. Al/Si* = bulk Al/Si

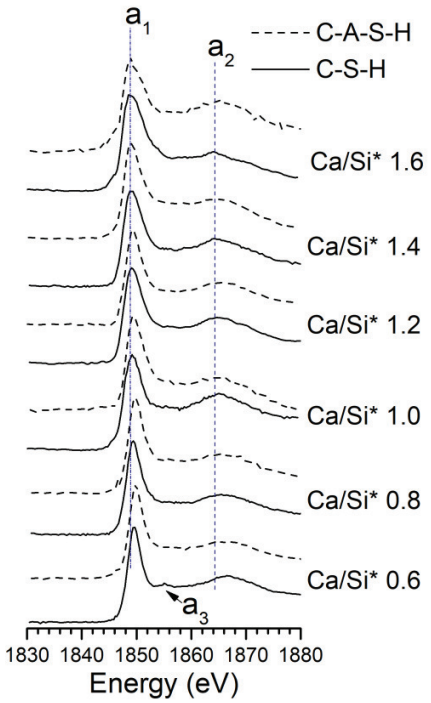

Figure 4. Si *K*-edge XANES spectra of C-S-H (solid lines) and C-A-S-H with Al/Si* = 0.05 (dashed lines) after 182 days of equilibration at 20 °C. Ca/Si* = bulk Ca/Si. Al/Si* = bulk Al/Si.

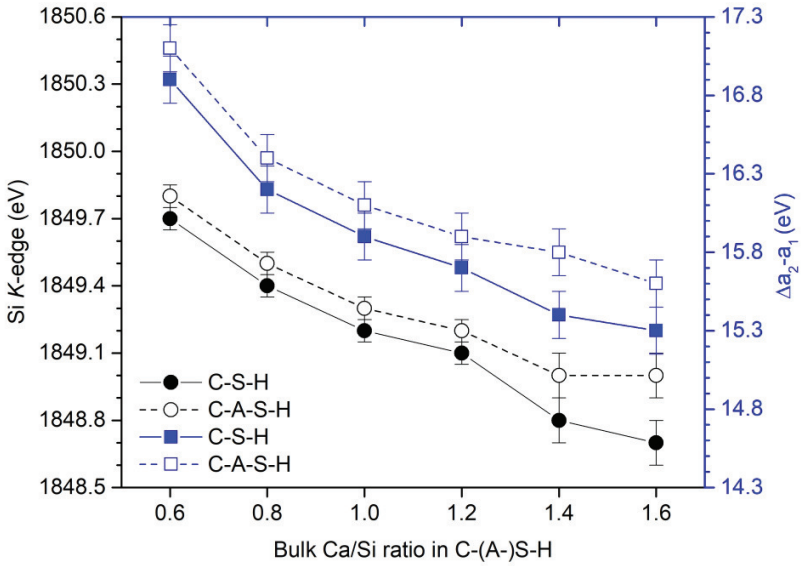

Figure 5. Si *K*-edge energy and energy separation between major and minor peak (Δa_2-a_1) as a function of Ca/Si* ratio of C-S-H (solid lines) and C-A-S-H with Al/Si* = 0.05 (dashed lines) after 182 days of equilibration at 20°C.

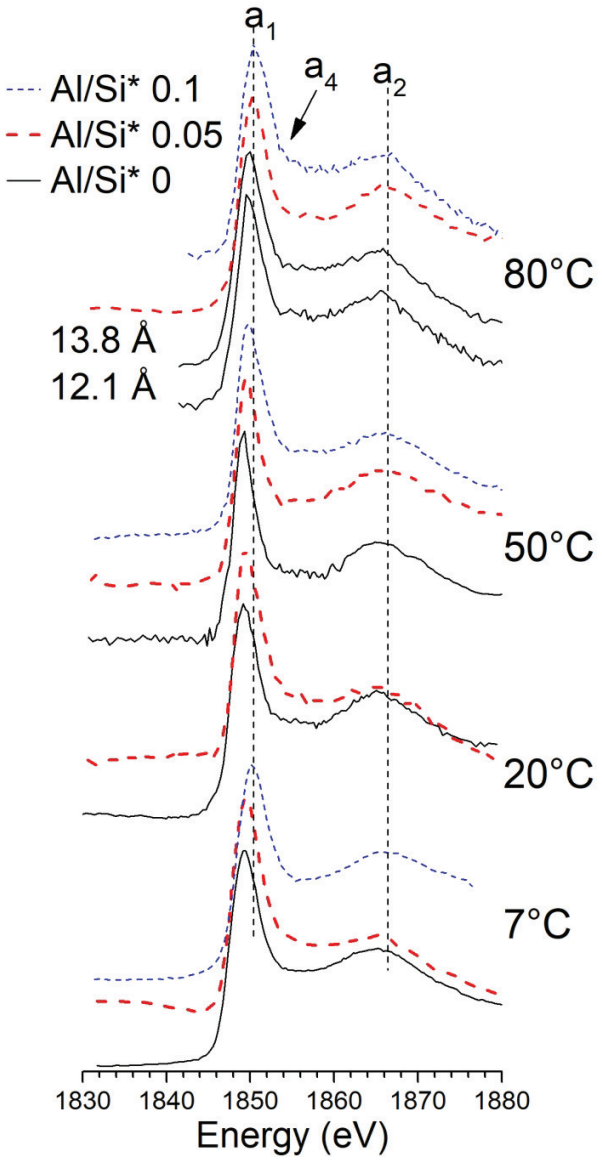

Figure 6. Si *K*-edge XANES spectra of C-S-H (solid lines, Ca/Si* = 1.0), C-A-S-H (red long-dashed lines, Al/Si* = 0.05, Ca/Si* = 1.0), and C-A-S-H (blue short-dashed lines, Al/Si* = 0.1, Ca/Si* = 1.0) at different equilibration temperatures. The two C-S-H phases exist in the 80 °C sample, which are labeled with their average basal spacings. Ca/Si* = bulk Ca/Si. Al/Si* = bulk Al/Si.

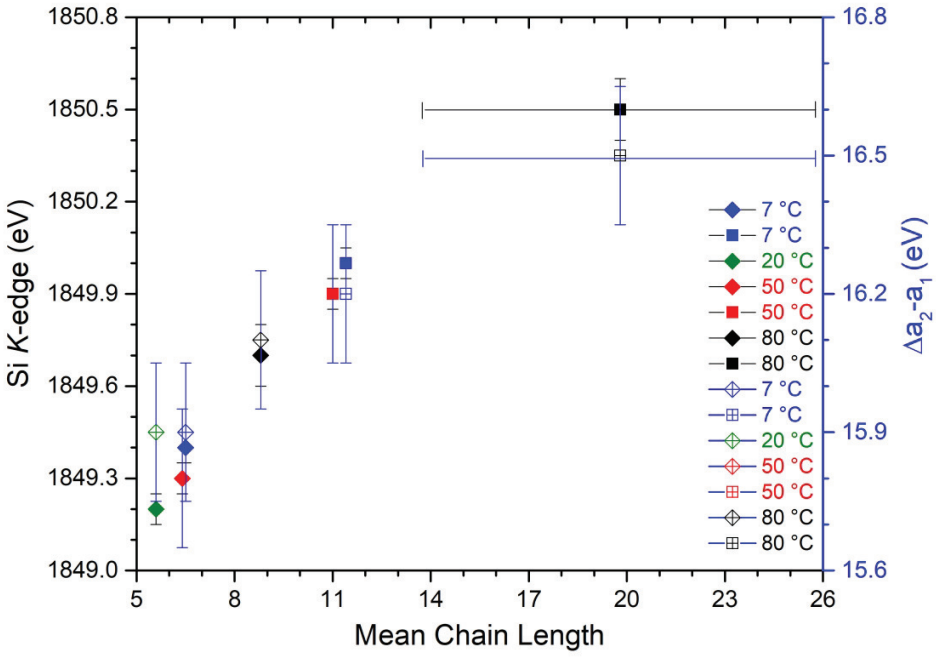

Figure 7. Si *K*-edge energy and energy separation between major and minor peak (Δa_2-a_1) as a function of the MCL of C-(A-)S-H equilibrated at 7-80 °C. The uncertainty of MCL (reproduced from [46]) is ± 1.25, except for the Al/Si* = 0.1 sample equilibrated at 80 °C, where the uncertainty of the MCL is represented by error bars. Al/Si* = 0.05 samples are marked as diamond and Al/Si* = 0.1 samples are marked as square. Al/Si* = bulk Al/Si.

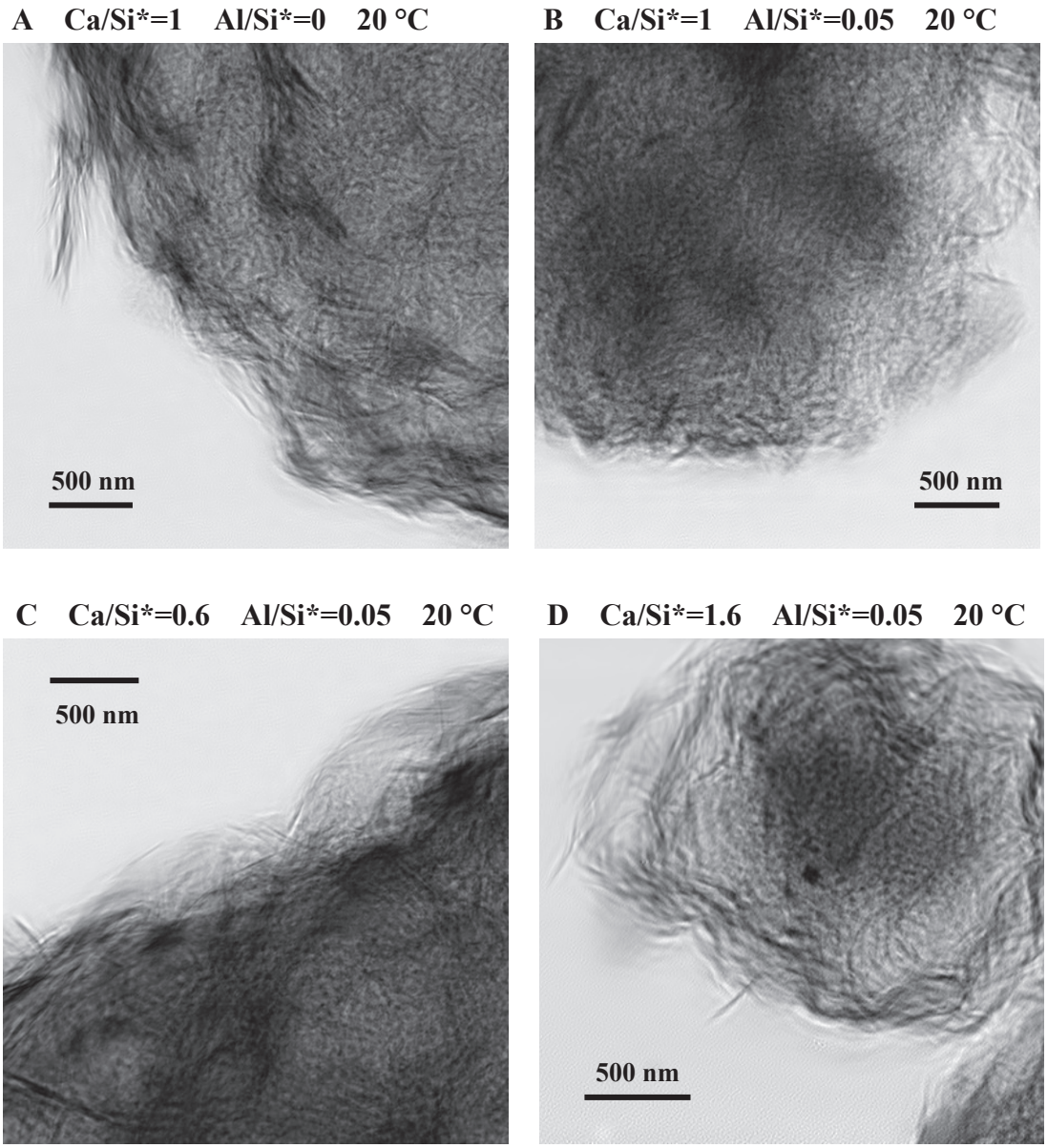

Figure 8. Ptychographic magnitude images of C-(A-)S-H equilibrated at 20 °C for 182 days: A) Ca/Si* = 1.0, Al/Si* = 0; B) Ca/Si* = 1.0, Al/Si* = 0.05; C) Ca/Si* = 0.6, Al/Si* = 0.05; and D) Ca/Si = 1.6, Al/Si* = 0.05. Ca/Si* = bulk Ca/Si. Al/Si* = bulk Al/Si.

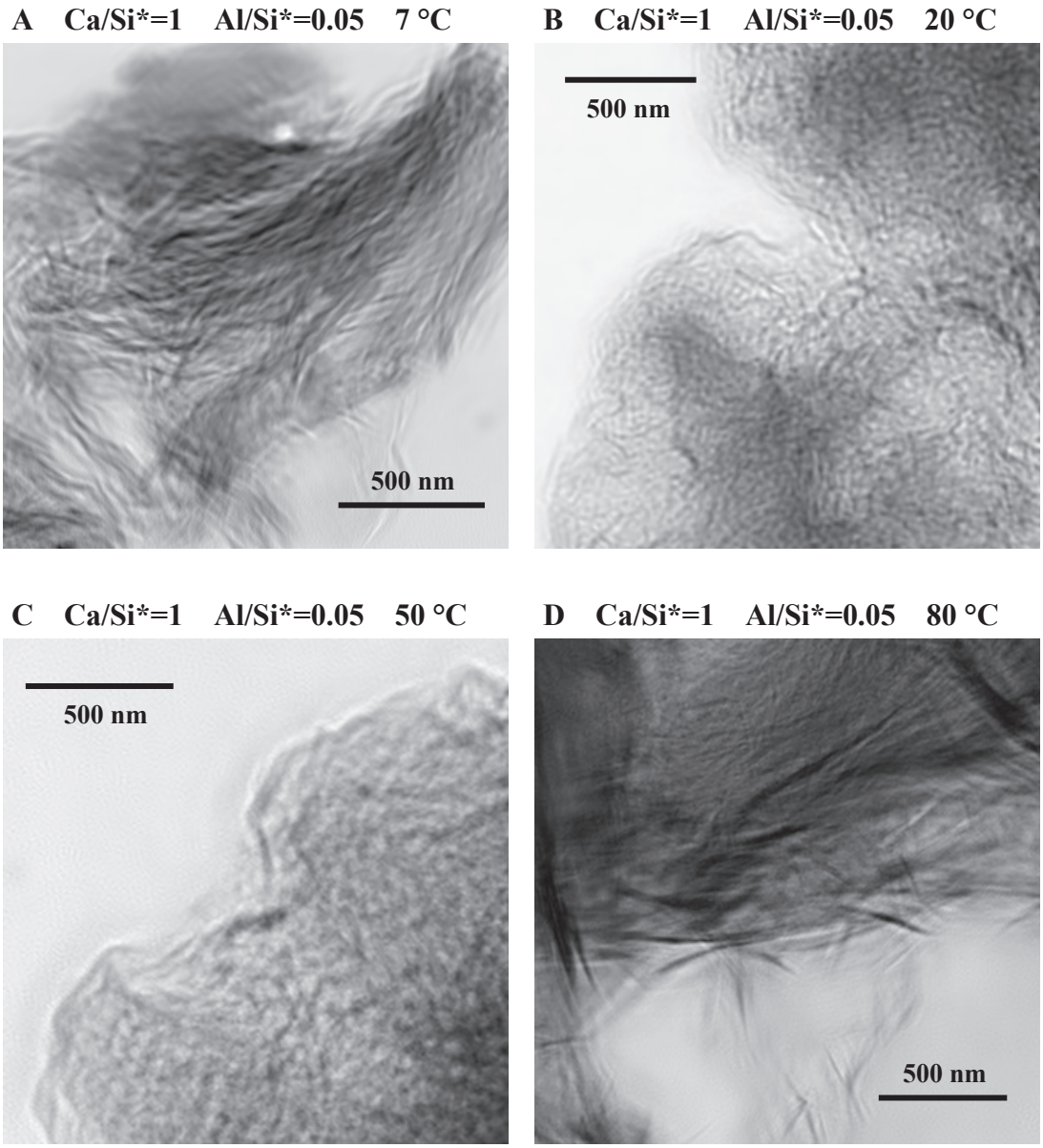

Figure 9. Ptychographic magnitude images of C-A-S-H with Ca/Si* = 1 and Al/Si* = 0.05; A) equilibrated for 365 days at 7 °C; B) equilibrated for 182 days at 20 °C; C) equilibrated for 56 days at 50°C; D) equilibrated for 56 days at 80°C.

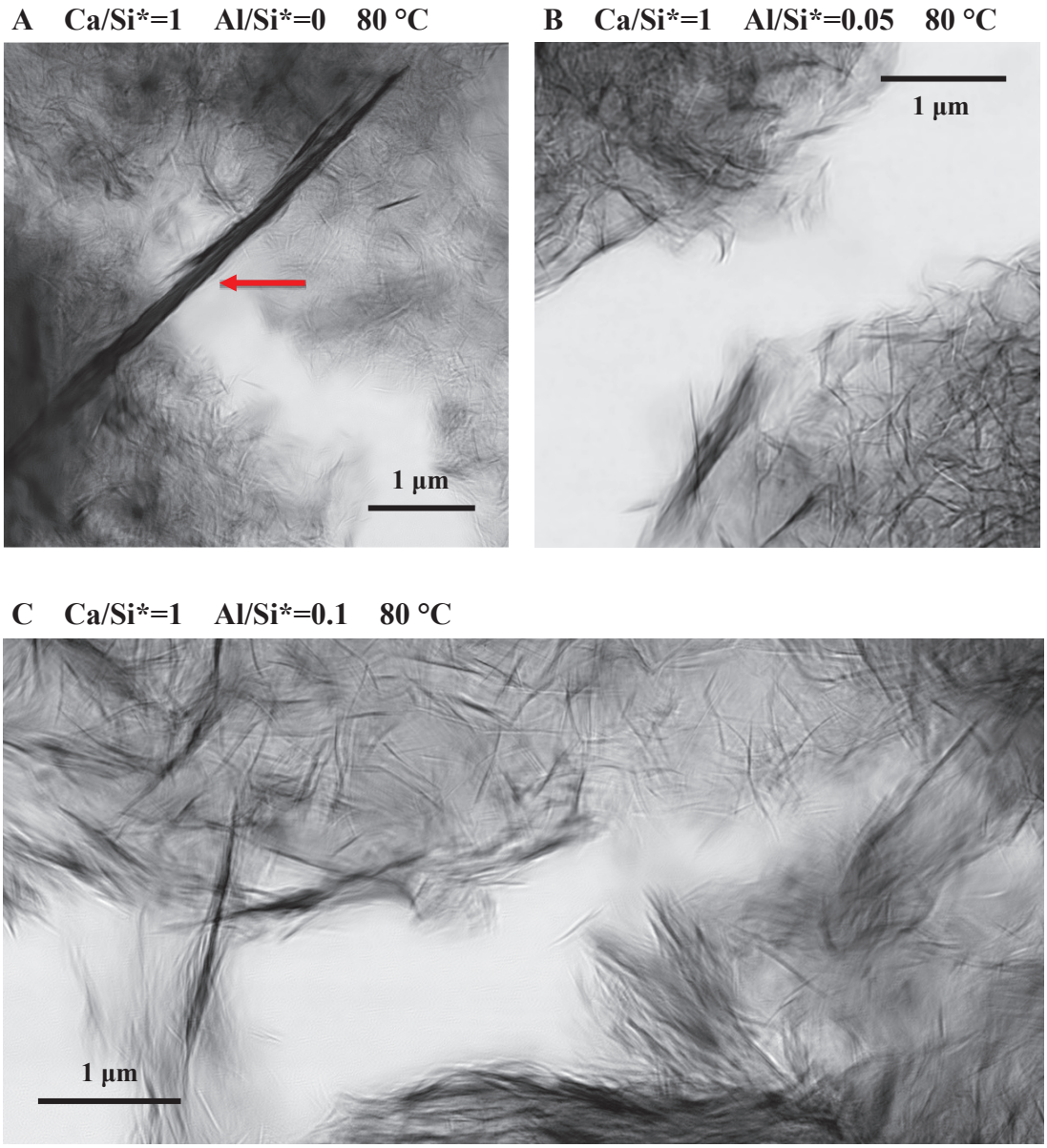

Figure 10. Ptychographic magnitude images of C-(A-)S-H equilibrated for 56 days at 80 °C: A) Ca/Si* = 1, Al/Si* = 0; B) Ca/Si* = 1, Al/Si* = 0.05; C) Ca/Si* = 1, Al/Si* = 0.1. Tobermorite crystal with an average basal spacing of 13.8 Å is indicated by a red arrow. Ca/Si*= bulk Ca/Si. Al/Si*= bulk Al/Si.

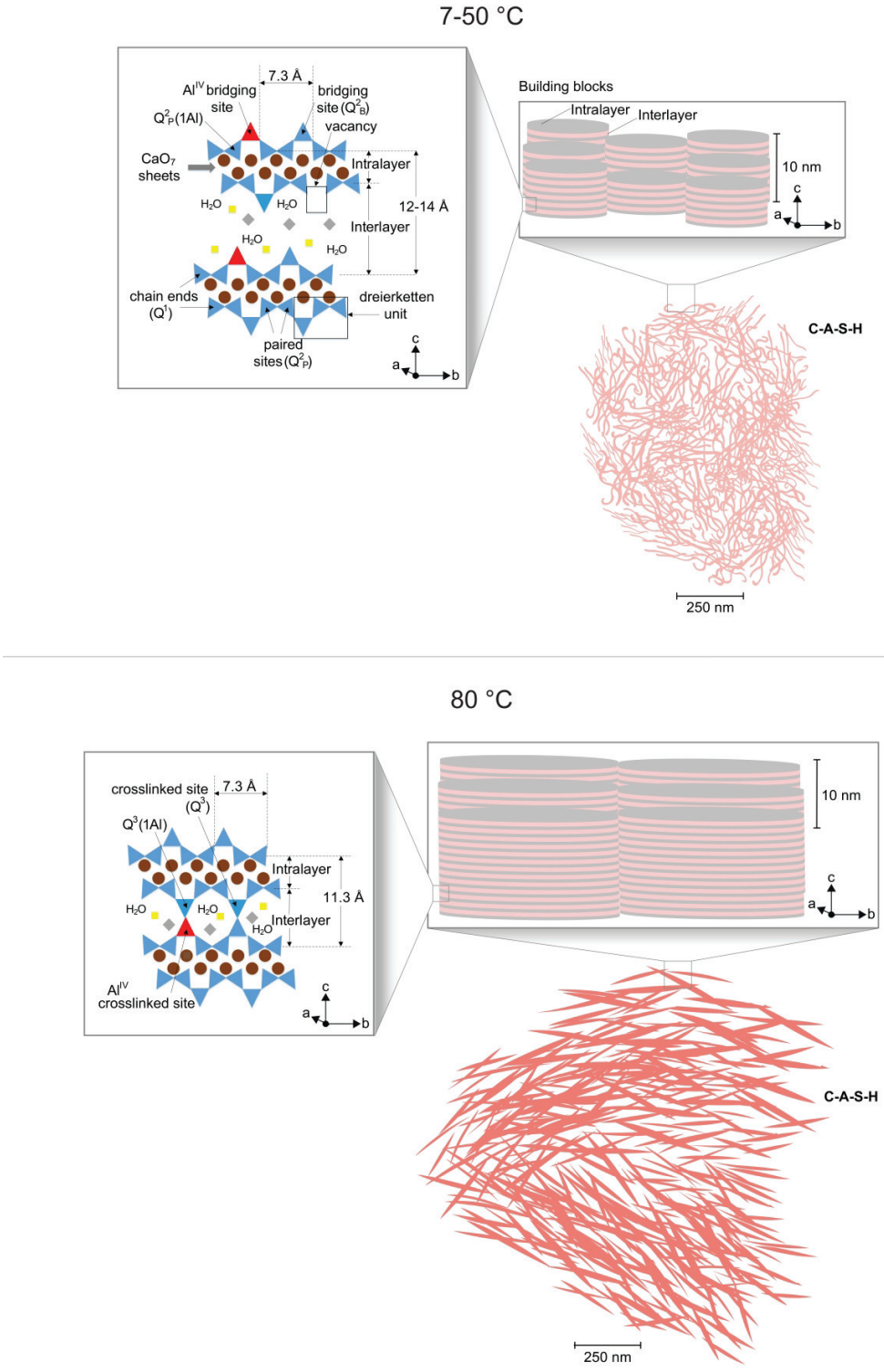

Figure 11. Schematic diagram of nanocrystalline C-A-S-H (equilibration temperature of 7 to 80°C). Brown circles represent Ca species in the CaO_7 sheets, and blue and red triangles denote SiO_4 and AlO_4 tetrahedron sites, respectively. The grey diamonds and

yellow squares are counterions (e.g., Ca species and five-fold coordinated Al species) in the interlayer. Pink and grey alternating stacked layers of the building blocks represent interlayer and intralayer, respectively. Rouge foils denote the networking structure of C-A-S-H at the nanoscale.

Supporting information for:

The Chemistry and Structure of Calcium (Alumino) Silicate Hydrate: A Study by XANES, Ptychographic Imaging, and Wide- and Small- Angle Scattering

Jiaqi Li[a,1], Guoqing Geng[a,b,1], Rupert Myers[a,c], Young-Sang Yu[d], David Shapiro[d], Carlo Carraro[e], Roya Maboudian[e], and Paulo J.M. Monteiro[a,f]

[a] Department of Civil and Environmental Engineering, University of California, Berkeley, California, United States

[b] Paul Scherrer Institute, Villigen, Switzerland

[c] School of Engineering, University of Edinburgh, Edinburgh, United Kingdom

[d] Advanced Light Source, Lawrence Berkeley National Laboratory, Berkeley, California, United States

[e] Department of Chemical and Biomolecular Engineering, University of California, Berkeley, California, United States

[f] Material Science Division, Lawrence Berkeley National Laboratory, Berkeley, California, United States

Appendix A. Wide Angle X-ray Scattering

The Wide Angle X-ray Scattering (WAXS) experiment was conducted at Beamline 1.3W at Synchrotron Light Research Institute (SLRI) in Thailand, using X-ray with machine energy of 9

[1] Corresponding authors
E-mail address: Jiaqi.li@berkeley.edu (J. Li) guoqing_geng@berkeley.edu (G. Geng)
Postal address: 115 Davis Hall, University of California at Berkeley, Berkeley, California, USA, 94720

keV, which corresponds to a wavelength of about 0.1378 nm, and a current of about 100 mA. Kapton film was cut and placed under the stainless steel sample holder. The dry C-A-S-H samples were dusted on the Kapton copper films evenly and covered the 1cm x 1cm apertures with a thickness of about 0.5mm. Another piece of Kapton film was placed on the other side of the sample holder. A blank sample holder with two stuck Kapton films was measured to subtract the scattering of Kapton film as background in the specimens. The sample holders were placed into the slit of the beamline and the samples were measured at lab-condition pressure and temperature. The sample-to-detector distance of WAXS measurement was 0.094m and its effective Q-range is 4.38-32.12nm^{-1}.

Table A1 Average (002) basal spacing and chemical composition in molar ratio of the C-(A-)S-H samples, and phases in solid assemblages of C-(A-)S-H systems

Initial molar ratio		Measured molar ratio			Average basal spacing, $d_{(002)}$ (Å) ±0.05	Katoite	Strätlingite	Portlandite
Ca/Si*	Al/Si*	Ca/Si	Al/Si	Ca/(Al+Si)				
Temperature 20°C								
0.8	0	0.80	-	0.8	13.63	-	-	-
	0.05	0.81	0.051	0.77	13.74	-	-	-
1.0	0	0.98	-	0.98	12.49	-	-	-
	0.05	0.99	0.05	0.94	12.80	-	-	-
1.6	0	1.38	-	1.38	9.56	-	-	Minor
	0.05	1.43	0.05	1.36	12.40	-	-	Minor
Temperature 7°C								
1.0	0	0.99	-	0.99	11.87	-	-	-
	0.05	0.98	0.044	0.94	12.49	Minor	-	-
	0.1	0.98	0.09	0.90	13.19	Minor	Minor	-
Temperature 50°C								

0	0.99	-	0.99	12.63	-	-	-
0.05	0.99	0.05	0.94	12.60	-	-	-
0.1	0.96	0.086	0.88	13.63	Minor	-	-
Temperature 80°C							
0	0.99	-	0.99	12.13, 13.76	-	-	-
0.05	0.99	0.05	0.94	11.43	-	-	-
0.1	0.99	0.1	0.90	11.37	-	-	-

Final bulk molar ratios are reproduced from [1, 2]

Appendix B. Additional ptychographic image.

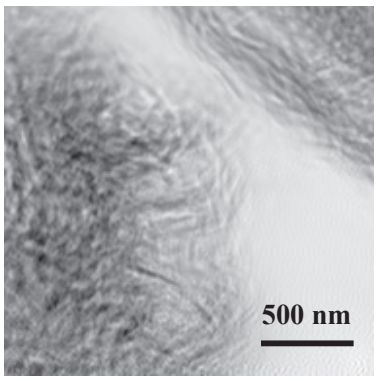

Supplementary Figure S1. Ptychographic image C-A-S-H (Ca/Si* = 1.2, Al/Si* = 0.05, hydration of 182days at 20°C) Ca/Si* = bulk Ca/Si. Al/Si* = bulk Al/Si.

Appendix C. Quantitative analysis of the ptychographic images.

The calculation of small angle scattering (SAS) from transmission images has been successfully used to quantify morphological information. The algorithm used in the present work has been well-described in [3] and was applied to the ptychographic images. A lamellar Guinier-Porod

model [4] was used to fit the calculated SAS. The fitting model contains a low-q Guinier region and a high-q linear Porod region, and the two regions intersect at q_1:

$$I(q) = \frac{G}{q^s}\exp\left[-\frac{q^2 \times (d-s)}{2q_1^2}\right]; \text{for } q \geq q_1 \quad (1)$$

$$I(q) = \frac{G}{q^d}\exp\left[-\frac{(d-s)}{2}\right] \times q^{(d-s)} \text{ for } q \leqslant q_1 \quad (2)$$

$$T = \frac{12^{0.5}}{q_1}\left[\frac{(d-s)(3-s)}{2}\right]^{0.5} \quad (3)$$

where q is the scattering variable; I(q) is the scattered intensity; d is the Porod exponent; G is the Guinier scale factor; and T is the thickness of layered scattering materials. The parameter s, 2, is used to model lamellar objects in the case of C-(A-)S-H building blocks.

The calculated SAS of ptychographic images (Figures 8, 9, 10 and S1) are plotted in Supplementary Figure S2 and S3.

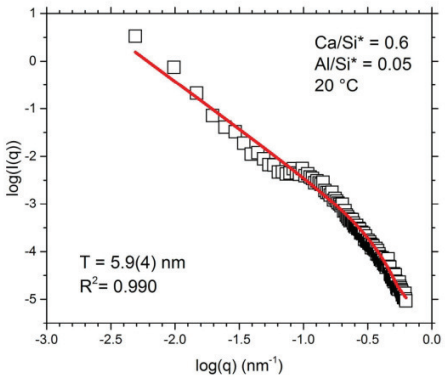

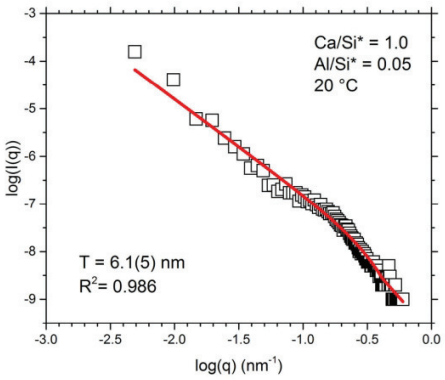

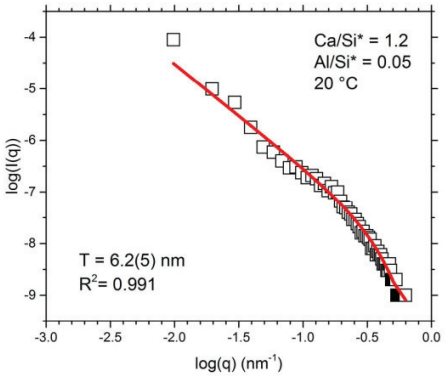

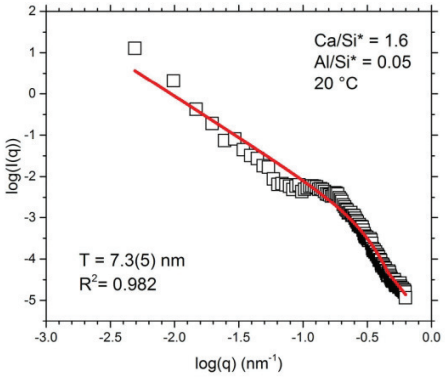

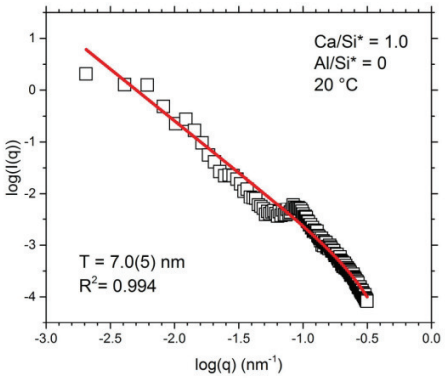

Supplementary Figure S2. Fitting of SAS data from images of C-(A-)S-H (equilibration temperature of 20°C). Fitted layer thickness (T) and coefficient of determination (R^2) of the

fitting are indicated in the plots. Estimated standard deviation of the thickness is shown in parentheses. Ca/Si*= bulk Ca/Si. Al/Si*=bulk Al/Si

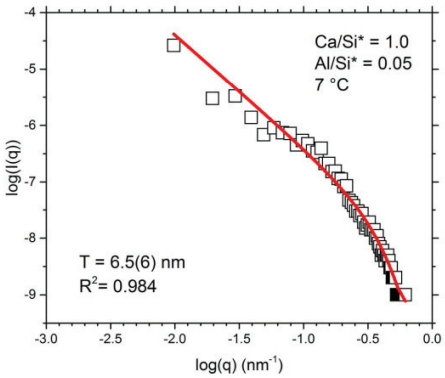

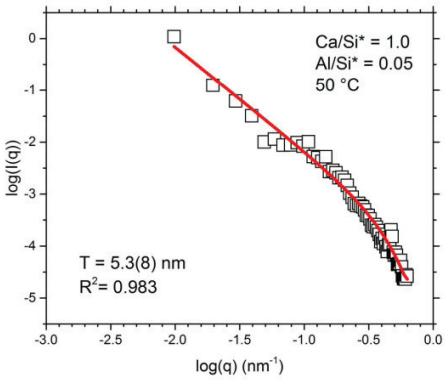

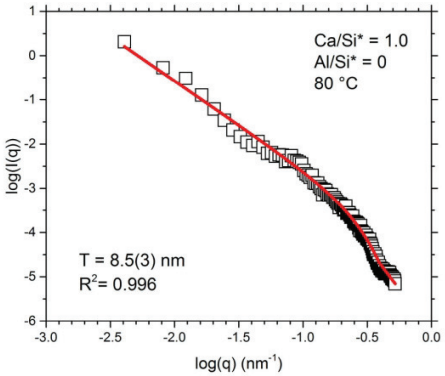

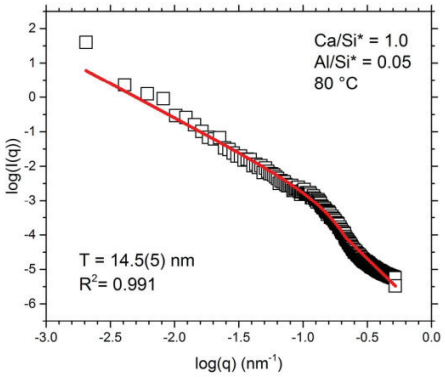

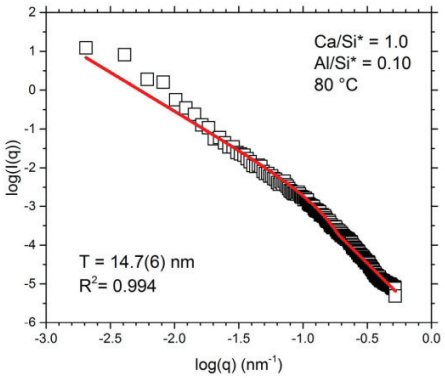

Supplementary Figure S3. Fitting of SAS data from images of C-(A-)S-H (equilibration temperatures of 7, 50, and 80°C). Fitted layer thickness (T) and coefficient of determination (R^2) of the fitting are indicated in the plots. Estimated standard deviation of the thickness is shown in parentheses. Ca/Si*= bulk Ca/Si. Al/Si*=bulk Al/Si

Supporting Information References

1. Myers, R.J., et al., *Effect of temperature and aluminium on calcium (alumino)silicate hydrate chemistry under equilibrium conditions.* Cement and Concrete Research, 2015. **68**: p. 83-93.
2. L'Hôpital, E., et al., *Influence of calcium to silica ratio on aluminium uptake in calcium silicate hydrate.* Cement and Concrete Research, 2016. **85**: p. 111-121.
3. Geng, G., et al., *Aluminum-induced dreierketten chain cross-links increase the mechanical properties of nanocrystalline calcium aluminosilicate hydrate.* Scientific Reports, 2017. **7**: p. 44032.
4. Hammouda, B., *A new Guinier–Porod model.* Journal of Applied Crystallography, 2010. **43**(4): p. 716-719.